Abstract

This thesis concerns describing the mechanical properties of the two dimensional material graphene by continuum elasticity theory. In particular, Nano ElectroMechanical Systems (NEMS) where part of the graphene sheet is made suspended, are considered.

In the first paper, the motion of a suspended graphene sheet is used to enhance the operation of a carbon nanotube field effect transistor. Here, the suspended graphene is used as a top-gate, controlling the charge density on the carbon nanotube channel. It is shown that the motion of the graphene sheet increases the sensitivity of the charge density on the carbon nanotube to the applied gate voltage.

A factor limiting the applicability of mechanical resonators in electronics is damping of the mechanical motion. In an ongoing project, a specific mode of dissipation, namely the coupling between the flexural motion of the graphene sheet to phonons in the graphene and the underlying substrate, is investigated on a theoretical basis. It is found that this mechanism gives rise to both linear and amplitude dependent (nonlinear) damping.

In paper II, the rigidity of graphene toward bending is investigated in collaboration with an experimental group at Gothenburg University. Here, compressive strain was built up in the graphene membrane through thermal cycling. Upon making the membrane suspended, the strain was released, causing the graphene to buckle. This type of buckled structures display an instability at a certain critical pressure. This critical pressure was then related to the bending rigidity of graphene. The bending rigidity was measured both for bilayered and monolayered graphene, with the result $\kappa_{Bi} \approx 30^{+20}_{-15}$eV and $\kappa_{Mono} \approx 7^{+4}_{-3}$ eV.

Keywords: Graphene, NEMS, Continuum elasticity

Contents

Chapter 1

Introduction

Carbon is the basis for all life on earth. Indisputably, one of the reasons for this is the remarkable diversity of the different forms of carbon, resulting from the versatility of its chemical bonds. This allows for recycling the individual carbon atoms within an organism; the same atom can, depending on how it is bonded, be a part of the neurons firing while you are reading this thesis, or of the muscle tissue in your fingers activated as you turn the pages. This diversity is seen also in pure carbon, or *carbon allotropes*. As an example, diamond is hard, transparent and insulating, while graphite is soft, opaque and conducting.

In the past decades, the possibility to apply carbon to our ever increasing technological demands have sparked a lot of interest. It has in particular focussed on a few remarkable discoveries of carbon allotropes existing on the nanoscale, starting with the so called ”Buckyballs” in 1985 [1], tiny balls of carbon where the atoms are arranged in the same way as the patches of a football. Single walled carbon nanotubes, tubes of carbon in the same characteristic hexagonal, or ”honeycomb” lattice as the graphite planes, were discovered in 1993 [2], although the tubular nature of carbon filaments was known much earlier [3]. Carbon nanotubes have the clear advantage over buckyballs that they can much more easily be connected to electrodes, simplifying using them in electronic applications. The next major discovery was made by Geim and Novoselov at Manchester University in 2004 [4], when they successfully isolated and characterised graphene, a single layer of graphite.

All these variations of carbon on the nanoscale show an impressive diversity of properties, but to fully exploit the possibilities of nanoscale carbon it is clear that a fundamental understanding of the physics underlying these properties must be developed. This thesis concerns the mechanical properties of graphene, described using classical continuum elasticity theory. This is the very same theory that underlies the equations of structural mechanics, beams and plates. However, as will be shown in this thesis, when applied to the two-dimensional material graphene, some interesting results arise.

1.1 Graphene

Graphene is a two-dimensional sheet of carbon atoms in a honeycomb structure (figure 1.1). In the original experiment of Geim and Novoselov, graphene was isolated by repeatedly splitting stacked graphite layers by the use of Scotch tape [4]. This method is still frequently in use, although much current research is focussed on growing graphene chemically, to allow for industrialisation of graphene growth [5].

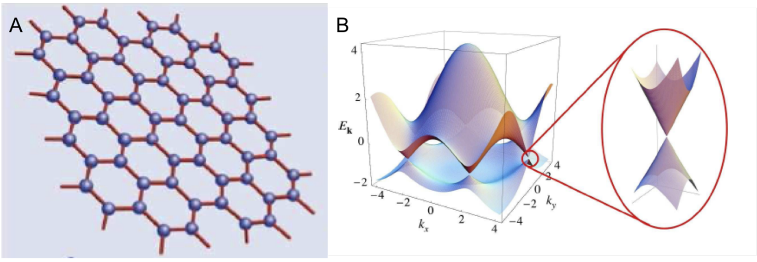

Figure 1.1: A: Schematic image of a graphene sheet, showing the carbon atoms arranged in a hexagonal lattice. B: The electronic spectrum of graphene, showing the linear spectrum close to the Dirac point as an inset. Image adapted from [6].

The properties of graphene differ significantly from conventional three-dimensional materials. Chemically, the bonds are constructed by hybridising two p-orbitals and one s-orbital (sp^2-hybridisation). The resulting chemical bond is referred to as a σ-bond, the most stable type of covalent bond. This is responsible for the remarkably high tensile strength of graphene. The remaining p-orbital may combine with free p-orbitals of neighboring carbon atoms to form a π-bond. These bonds are in turn what determines the electronic properties of graphene.

Among the most extraordinary features of the electronic properties of graphene is its linear spectrum close to the Fermi energy,

$$E = \pm\hbar v_F k,$$

with k measured from the so called Dirac point. The spectrum is conical with edges at the six corners of the Brillouin zone of the hexagonal lattice (figure 1.1). Physically, this means that the velocity of the electrons, $v = \frac{1}{\hbar}\frac{\partial E}{\partial k} = v_F$ is constant, independent of momentum, close to the Fermi energy. The Fermi velocity in graphene is $\sim 10^6$ m/s meaning that at short distances electrons in graphene move like massless particles at about 1% of the speed of light. In fact, the electrons in this region obey the massless Dirac equation, and are therefore often referred to as massless Dirac fermions. At distances longer than the mean free path of the electrons, the charge transport is diffusive with reported electron mobilities up to 150000 $\mathrm{cm^2V^{-1}s^{-1}}$ at room temperature [7, 8].

For a thorough overview of the electronic properties of graphene, the reader is referred to the review by Castro Neto et al. [6].

1.2 Graphene and Nano ElectroMechanical Systems (NEMS)

In recent years there has been considerable interest in combining the mechanical and electrical properties of carbon allotropes on the nanoscale in so called Nano ElectroMechanical Systems (NEMS). A prototypal NEMS device is depicted in figure 1.2. A graphene sheet is suspended over a trench, and is actuated by applying a voltage to the gate below it. Nano electromechanical systems are a miniaturised extension of the widely employed microelectromechanical systems (MEMS) developed in the 1980s. There is a wide range of enticing applications of carbon based NEMS, such as mass detectors with resolution reaching 10^{-21} g [9], nano electromechanical switches [10, 11], tunable RF resonators [12, 13], memory devices [14] and transducers acuating and detecting mechanical motion on the nanoscale [15]. Also, these structures pave the way for experimental detection of quantised mechanical motion [16]. In an article not included in this thesis, it is shown that carbon nanotube resonators coupled to a quantum dot in a so called single electron transistor can display a parametric instability. Then, the mechanical response of the resonator is large in a narrow frequency range. This could be used in filtering applications [17].

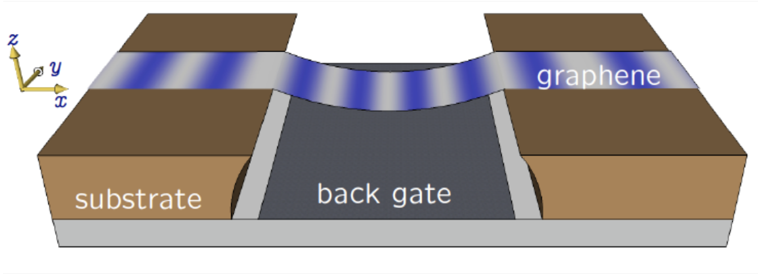

Figure 1.2: A prototypal graphene NEMS structure. A graphene sheet is supended over a trench in the substrate. Mechanical motion of the graphene is induced by applying a voltage to the gate below it.

Using graphene in NEMS has both advantages and drawbacks. The combination of high tensile strength and low mass enables mechanical resonance frequencies at the gigaherz scale [18]. The low mass and high electron mobility also reduce energy consumption, which will increase importance with increasing technological demands.

On the other hand, pure graphene lack the band gap of conventional semiconductors. The conductivity of the graphene sheet can be tuned by changing the charge concentration on it, just as in a regular semiconductor, but unlike regular semiconductors the conductivity of graphene never quite vanishes. This is a major drawback in applications where a low off-state current is required, such as in logical applications. This can be circumvented by for instance using bilayer graphene (two graphene sheets stacked on top of each other) or two graphene sheets with a semiconducting material in between [19]. In paper I of this thesis a different approach is used. The charge channel is there a semiconducting carbon nanotube, which has the desired band gap. The conductivity of the nanotube is then tuned by a flexible top gate made of graphene. This is investigated in chapter 3.

In chapter 4 the concept of dissipation is introduced, and a specific mode of dissipation, namely the coupling between out-of-plane and in-plane motion of the graphene is analysed. In the last chapter, the rigidity of graphene sheets to bending is investigated. Here, the instability of shallow shells under external pressures is used to estimate the bending rigidity of bilayered and monolayered graphene.

1.3 Limitations of elasticity theory on graphene

The theory of elasticity has been used extensively the past centuries to describe the structural properties of solids. Still 250 years after its formulation engineers use the Euler-Bernoulli equation to calculate the deflection of loaded beams, and the Kirchoff-Love equations to estimate the vibrations of plates.

Despite the enormous success of the theory, it is by no means obvious that the classical theory is accurate in the two dimensional material graphene. In fact, to lowest order in the free elastic energy graphene would inevitably crumple and disintegrate, thus being highly unstable. Although this is solved going to nonlinear terms in the free energy, the nonexistence of graphene as a stable form of carbon in the standard linear formulation of elasticity theory calls to question the validity of applying those equations to graphene. Nonetheless, elasticity theory has proven to describe most of the mechanical properties of graphene remarkably well.

It is worth noting, that it is in the rare cases where elasticity theory breaks down that the new and exotic mechanical properties of the two-dimensional membrane typically emerges, such as the negative thermal expansion coefficient [20] or the non-vanishing bending rigidity, which will be discussed in section 5. Despite the fact that some macroscopic properties of graphene cannot be accurately derived from continuum elasticity theory alone, elasticity theory is in many cases a useful framework for modeling graphene with the macroscopic parameters as input. Furthermore, being able to describe the mechanical properties of graphene using a simple set of equations immensely simplifies the transition from scientific studies to commercial applications of graphene. Charting the applicability space of elasticity theory on graphene is therefore a very important field of study.

Chapter 2

Elasticity theory

The aim of this section is to give a short review on the elasticity theory used in the thesis. In the process, the equations of motion for a graphene sheet under external forcing are derived. The discussion follows the book of Landau and Lifshitz [21].

When an elastic body is deformed, the distance between points in the body is changed. A measure of the deformation is then the difference between the squared length element in the deformed body (dX_I) and the undeformed body (dx_i)

$$dX_I dX_I - dx_i dx_i = \frac{\partial X_I}{\partial x_j}\frac{\partial X_I}{\partial x_k} dx_j dx_k - dx_i dx_i = \left(\frac{\partial X_I}{\partial x_j}\frac{\partial X_I}{\partial x_k} - \delta_{jk} \right) dx_i dx_k \tag{2.1}$$

where summation over repeated indicies is implied. Defining the *displacement field* as

$$u_j = X_j - x_j, \tag{2.2}$$

the difference in length elements can be written as

$$dX_I dX_I - dx_i dx_i = \left(\frac{\partial u_i}{\partial x_j} + \frac{\partial u_j}{\partial x_i} + \frac{\partial u_l}{\partial x_i}\frac{\partial u_l}{\partial x_j} \right) dx_i dx_j = 2\epsilon_{ij} dx_i dx_j. \tag{2.3}$$

Here ϵ_{ij} is the *strain tensor*,

$$\epsilon_{ij} = \frac{1}{2}\left(\frac{\partial u_i}{\partial x_j} + \frac{\partial u_j}{\partial x_i} + \frac{\partial u_l}{\partial x_i}\frac{\partial u_l}{\partial x_j} \right). \tag{2.4}$$

The free energy density for a deformed elastic body can, to lowest nonvanishing order in the strain tensor, be written as

$$F = \frac{\lambda}{2}\epsilon_{ii}\epsilon_{jj} + \mu\epsilon_{ij}\epsilon_{ij} \tag{2.5}$$

where λ and μ are known as the Lamé parameters of the material. The internal stresses in the elastic body are given by the stress tensor,

$$\sigma_{ij} = \frac{\partial F}{\partial \epsilon_{ij}}. \tag{2.6}$$

This gives a linear relation between the strain and the stress in a material, and it is a three dimensional generalisation of Hooke's law.

In the following, we take the elastic body to be a two dimensional sheet extended in the x-y plane. The strain tensor will then only have three components, so the free energy expression takes the form

$$F = \frac{\lambda}{2}\epsilon_{ii}^2 + \mu\epsilon_{ij}^2 = \left(\frac{\lambda}{2} + \mu\right)\left(\epsilon_{xx}^2 + \epsilon_{yy}^2\right) + \lambda\epsilon_{xx}\epsilon_{yy} + \mu\epsilon_{xy}^2, \tag{2.7}$$

Denoting the displacement fields by

$$u_x = u(x,y), \quad u_y = v(x,y), \quad u_z = w(x,y), \tag{2.8}$$

the components of the strain tensor are, to lowest nonvanishing order in the displacement fields,

$$\begin{aligned} \epsilon_{xx} &= \partial_x u + \frac{1}{2}(\partial_x w)^2, \\ \epsilon_{yy} &= \partial_y v + \frac{1}{2}(\partial_y w)^2, \\ \epsilon_{xy} &= \frac{1}{2}\left(\partial_y u + \partial_x v + \partial_x w \partial_y w\right). \end{aligned} \tag{2.9}$$

Higher order terms of the in-plane displacements have been omitted. This approximation will be denoted the membrane approximation, and will be investigated in chapter 4 on nonlinear dissipation in suspended graphene. As an instructive example we make a further approximation for the moment,

$$\partial_x u = \partial_y u = \partial_x v = \partial_y v = \delta_0. \tag{2.10}$$

This approximation is valid for suspended membranes with large, homogeneous initial strain δ_0. In graphene, this strain is often rather large due to stresses in the material during the mechanical exfoliation procedure. This approximation is referred to as the out-of-plane approximation, as the in-plane displacements are assumed to be void of dynamics. The free energy density becomes

$$\begin{aligned} F = &\left(\frac{\lambda}{2} + \mu\right)\left(2\delta_0^2 + \delta_0\left((\partial_x w)^2 + (\partial_y w)^2\right) + \frac{1}{4}(\partial_x w)^4 + \frac{1}{4}(\partial_y w)^4\right) \\ &+ \lambda\left(\delta_0^2 + \frac{\delta_0}{2}\left((\partial_x w)^2 + (\partial_y w)^2\right) + \frac{1}{4}(\partial_x w)^2(\partial_y w)^2\right) \\ &+ \mu\left(\delta_0^2 + \delta_0 \partial_x w \partial_y w + \frac{1}{4}(\partial_x w \partial_y w)^2\right). \end{aligned} \tag{2.11}$$

The Lagrangian density of this system is therefore given by

$$\mathcal{L} = \rho\frac{\dot{w}^2}{2} - F. \tag{2.12}$$

Applying the Euler-Lagrange equations on the Lagrangian, using the free energy given by (2.11) results in the equation of motion for suspended graphene sheets in the current approximation,

$$\rho\ddot{w} - T_0\nabla^2 w - T_1\partial_x\left((\partial_x w)|\nabla w|^2\right) - T_1\partial_y\left((\partial_y w)|\nabla w|^2\right) = f(x, y, t) \tag{2.13}$$

where $T_1 = \lambda + 2\mu$ is a construction from the Lamé parameters, $T_0 = T_1\delta_0$, and $f(x, y, t)$ is an applied force density. We note that the linear wave equation is recovered for $T_0 \gg T_1$. In most applications however, T_0 is much smaller than T_1, meaning that the response of a suspended graphene sheet is highly nonlinear. The type of this nonlinearity is more transparent when looking at the dynamics of a single mode of the graphene sheet. We assume that only one mode is excited and write $w(x, y, t) = q(t)\phi(x, y)$, with $\phi(x, y)$ normalised to the area of the suspended sheet, $\int dxdy\phi(x, y)^2 = A$. The equation of motion then transforms to

$$\ddot{q} + \frac{T_0}{\rho A}q\int dxdy(\nabla\phi)^2 + \frac{T_1}{\rho A}q^3\int dxdy\,(\nabla\phi)^4 = \frac{1}{\rho A}\int dxdyf(x, y, t)\phi. \tag{2.14}$$

The qubic nonlinearity in the mode amplitude q is the hallmark of the Duffing oscillator. The resonance frequency is given by

$$\omega_0 = \sqrt{\frac{T_0}{\rho A}} \left(\int dxdy (\nabla\phi)^2 \right)^{1/2} \tag{2.15}$$

and the Duffing parameter given by

$$\alpha = \frac{T_1}{\rho A} \int dxdy \, (\nabla\phi)^4 \, . \tag{2.16}$$

In this model, the importance of nonlinearities in the response of graphene is determined on one hand by the ratio between the initial tension of the sheet and the intrinsic tensile strength, $\frac{T_0}{T_1}$, and on the other on the ratio of the overlap integrals of the excited mode, which is a purely geometrical factor. An important feature of the Duffing equation is that the resonance frequency is changed when the displacement of the membrane increases. This is most easily seen by linearising the equation around a static equilibrium, $q = q_0 + \delta q$. The linearised equation then becomes

$$\ddot{\delta q} + \left(\omega_0^2 + 3\alpha q_0^2\right) \delta q = \frac{1}{\rho A} \int dxdy f(x,y,t) \phi. \tag{2.17}$$

The resonance shift is therefore given by

$$\delta\omega^2 = 3\alpha q_0^2. \tag{2.18}$$

A more general mode expansion, $w(x,t) = q_0\phi_0(x,y) + \sum q_n(t)\phi_n(x,y)$ gives the result

$$\ddot{q}_n + \omega_n^2 q_n + 3\sum_{i,j} q_i q_j I_1(i,j,n) + \sum_{i,j,k} q_i q_j q_k I_2(i,j,k,n) = \frac{1}{\rho A} \int dxdy f(x,y,t)\phi_n(x,y) \tag{2.19}$$

where ω_n is the frequency of the n-th mode, and I_1 and I_2 are overlap integrals given by

$$\begin{aligned} I_1(i,j,n) =& \frac{q_0}{\rho A} \int_\Omega (\nabla\phi_0) \cdot (\nabla\phi_n) (\nabla\phi_i) \cdot (\nabla\phi_j) \, d\Omega \\ I_2(i,j,k,n) =& \frac{1}{\rho A} \int_\Omega (\nabla\phi_k) \cdot (\nabla\phi_n) (\nabla\phi_i) \cdot (\nabla\phi_j) \, d\Omega \end{aligned} \tag{2.20}$$

The overlap integrals couple the vibrational modes of the graphene sheet; if the coupling constants are nonzero, exciting one mode will inevitably excite other vibrational modes, effectively acting as a mode of dissipation. Other modes of dissipation with the same structure will be discussed in chapter 4.

Chapter 3

Modeling of graphene dynamics

In this chapter, the simplified equation of motion (2.13) derived in the previous chapter is investigated both analytically and numerically. Furthermore, the mechanical properties are coupled to the electrical properties of graphene, resulting in a simple model for a suspended graphene transistor.

The system at hand is depicted in figure 1.2. A graphene sheet is suspended between two electrodes, source and drain, over a back gate. When a voltage is applied to the back gate, the resulting electric field between the back gate and the suspended graphene sheet causes charge to accumulate on both surfaces, much as in a regular capacitor. This charge accumulation generates a force between the gate and the graphene, which in turn causes the graphene sheet to move.

As a first approximation, consider two static, parallel plates separated by a distance d. The voltages on the two plates are $\pm V/2$, respectively. The electric field between the plates is homogeneous and given by $E_z = \frac{V}{d}$. From Gauss law it follows that the charge on the plates are given by $Q = \pm\epsilon_0 \frac{AV}{d}$. The proportionality constant between the charges and the applied voltage is called the *capacitance* of the system. The force between the plates is given by the gradient of the electrostatic energy,

$$\mathbf{F} = -\nabla U = \frac{1}{2}\nabla V Q = \frac{1}{2}\frac{\partial C}{\partial z}V^2\hat{z}. \tag{3.1}$$

Note that taking the voltage V to be oscillating with frequency ω, the force oscillates at the double frequency, 2ω. The reason for this is that reversing the sign of the voltage does not reverse the sign of the force; the opposing charges on the two plates will still attract.

The equation of motion of the suspended graphene under the influence of a time dependent voltage on the back gate will therefore, in this approximation, be

$$\ddot{q}_n+\omega_n^2 q_n+3\sum_{i,j} q_i q_j I_1(i,j,n)+\sum_{i,j,k} q_i q_j q_k I_2(i,j,k,n)=\frac{1}{\rho A}\frac{\epsilon_0}{2d^2}V(t)^2\int dxdy\phi_n \tag{3.2}$$

The effect of this force acting on the graphene sheet will be that the graphene sheet starts to oscillate. However, when the graphene moves, the distance separating the graphene and the back gate will change, effectively changing the force acting on the graphene. To estimate this effect, consider a voltage signal consisting of a static part and a time varying part, $V(t)=V_{dc}+V_{ac}(t)$, $V_{dc}\gg V_{ac}$. To a first approximation the force would be given by

$$F[x,y,t,w]=\frac{\epsilon_0}{2(d-w)^2}(V_{dc}+V_{ac}(t))^2, \tag{3.3}$$

where w is the deviation from the equilibrium position of the graphene sheet. This force can be expanded in a Taylor series,

$$F[x,y,t,w]=\frac{\epsilon_0}{2d^2}(V_{dc}+V_{ac}(t))^2\sum_n n\left(\frac{w}{d}\right)^{n-1}. \tag{3.4}$$

Considering only the first two terms in this expansion, the equation of motion becomes

$$\begin{aligned}&\ddot{q}_n+\left(\omega_n^2-\frac{\epsilon_0}{\rho A d^3}V_{dc}^2\int dxdy\phi_n(x,y)\right)q_n+\\&3\sum_{i,j} q_i q_j I_1(i,j,n)+\sum_{i,j,k} q_i q_j q_k I_2(i,j,k,n)=\\&\frac{\epsilon_0}{2\rho A d^2}\left(V_{dc}^2+2V_{ac}V_{dc}\right)\int dxdy\phi_n(x,y)\end{aligned} \tag{3.5}$$

which implies that, to lowest order in the deflection q_0, the resonance frequency of each mode is reduced by the amount

$$\delta\omega_{el}^2=\frac{\epsilon_0}{\rho A d^3}V_{dc}^2\int dxdy\phi_n(x,y) \tag{3.6}$$

as a consequence of the electrostatic interaction between the graphene and the back gate. At the same time, from the single mode expansion (2.17) it is clear that the mechanical nonlinearities gives a renaormalisation of the frequency according to $\delta\omega_{mech}^2 = 3\alpha q_0^2$. It is worth noting, that when $\omega_0^2 - \delta\omega_{el}^2 + \delta\omega_{mech}^2 < 0$ where ω_0 is the frequency of the fundamental mode, the structure is unstable and the graphene sheet will "snap in" to the back gate.

The critical point is readily estimated within the single mode approximation, $w = (q_0 + \delta q(t))\phi(x, y)$. Here, q_0 is the equilibrium deformation resulting from the DC bias voltage and is given by solving the static equation of motion.

Let $\phi(x, y) = \sqrt{2}\cos(\pi x/l)$ be the fundamental mode for a doubly clamped nanoribbon. Then, the resonance frequency is given by (2.15),

$$\omega_0 = \frac{\pi}{l}\sqrt{\frac{T_0}{\rho}} \tag{3.7}$$

and the Duffing parameter

$$\alpha = \frac{\pi^4}{l^5}\frac{T_1}{\rho}. \tag{3.8}$$

The equation for the static bias point then becomes

$$\omega_0^2 q_0 + \alpha q_0^3 = \sqrt{2}\epsilon_0 \frac{V_{dc}^2}{\rho A(d - q_0)^2} \tag{3.9}$$

At the instability, the change in displacement due to a change in voltage diverges, i.e.

$$\frac{\partial q_0}{\partial V_{dc}} \to \infty \tag{3.10}$$

which gives the condition

$$0 = \omega_0^2 d - 3\omega_0^2 q_0 + 3\alpha d q_0^2 - 5\alpha q_0^3 \tag{3.11}$$

so in the absence of a Duffing nonlinearity, the sheet will snap in at $q_0 = d/3$. Adding the Duffing nonlinearity stabilises the sheet slightly, and for a strictly nonlinear sheet the snap in occurs at $q_0 = 3d/5$.

It should be noted that the above considerations are based on crude simplifications, and a more sophisticated analysis of the governing equations requires a numerical treatment. To resolve this issue, we divide the graphene into a triangular mesh. The charge density on each triangle is found by solving Maxwells equations using the Boundary Element Method (BEM).

The position of the sheet is then found by solving the equation of motion iteratively. In figure 3.1, the numerically extracted resonance frequency is shown as a function of bias voltage for a resonator of length $l = 1\mu$m, width $w = 1\mu$m, $\frac{T_0}{T_1} = 10^{-3}$ and gate distance $d = 400$nm. The slight decrease in resonance frequency for small values of the bias voltage is due to the electric softening $\delta\omega_{el}^2$, while the subsequent increase is a result of the mechanical stiffening $\delta\omega_{mech}^2$.

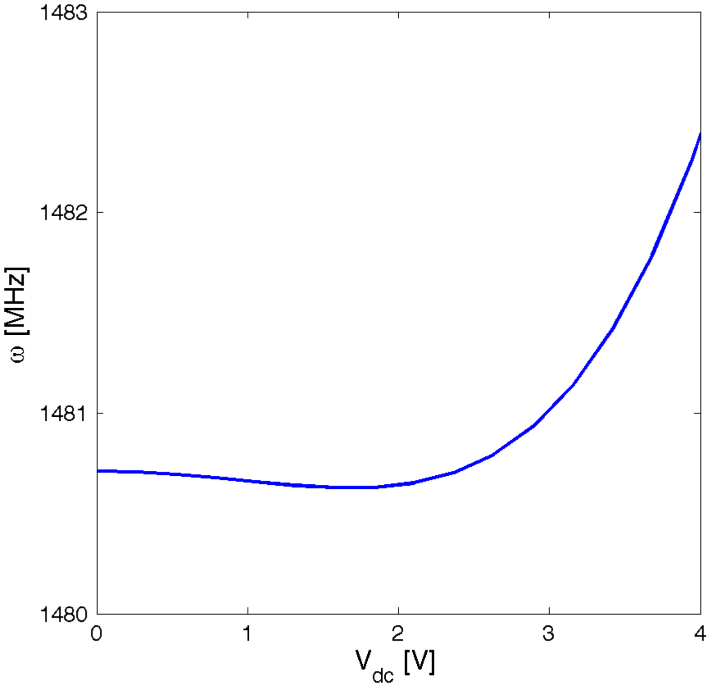

Figure 3.1: The resonance frequency of a suspended graphene sheet with parameters defined in the text, as a function of the bias voltage. The resonance frequency initially decreases slightly as a result of the electronic softening, but then increases again due to the mechanical stiffening of sheets under tension. For even higher frequencies, the electronic softening is expected to again prevail causing the sheet to snap-in to the substrate.

3.1 CNTFET with suspended graphene gate

Adding to the structure described so far a semiconducting carbon nanotube (CNT) between the graphene and the back gate, we have a field effect transistor (FET) with a flexible top gate (figure 3.2). This structure was realised and studied experimentally by Svensson et al. By changing the voltages on the back gate and the graphene top gate, the carrier density induced by the two gates, and with it the conductance, of the carbon nanotube is altered. The flexibility of the graphene top gate can easily be shown to increase the response of the device to an applied voltage: the charge induced on the CNT by a change of voltage on the top gate is

$$\delta Q_{CNT} = \delta(C_{gg}V_{gg}) = C_{gg}\delta V_{gg} + V_{gg}\delta C_{gg}, \tag{3.12}$$

where C_{gg} is the capacitance between the CNT and the graphene gate, and V_{gg} is the voltage on the top gate. However, the capacitance depends on the position of the graphene, which in turn depends on the voltage, so

$$\delta Q_{CNT} = \delta V_{gg}\left(C_{gg} + \frac{\delta C_{gg}}{\delta u}\frac{\delta u}{\delta V_{gg}}\right), \tag{3.13}$$

which is to be compared with the case of a static gate,

$$Q_{CNT}^{static} = C_{gg}\delta V_{gg}. \tag{3.14}$$

It is worth noting that the capacitance between the graphene gate and the back gate is neglected in this analysis.

3.1.1 Subthreshold slope

As a figure of merit of the structure we study the subthreshold slope (S^{-1}),

$$S^{-1} = \frac{\partial \lg\left(\frac{I_d}{I_0}\right)}{\partial V_{gg}}, \tag{3.15}$$

which is a measure of the variation of current due to a variation of the gate voltage. The logarithm is taken in base 10. Treating the system as a capacitive network, we have for the charge Q on the CNT-channel,

$$Q = C_{gg}(\xi(Q)/e - V_{gg}) + C_{bg}(\phi(Q) - V_{bg}) \Rightarrow \phi(Q) - \frac{Q}{C_{\sum}} = \frac{V_{gg}C_{gg} + V_{bg}C_{bg}}{C_{\sum}}, \tag{3.16}$$

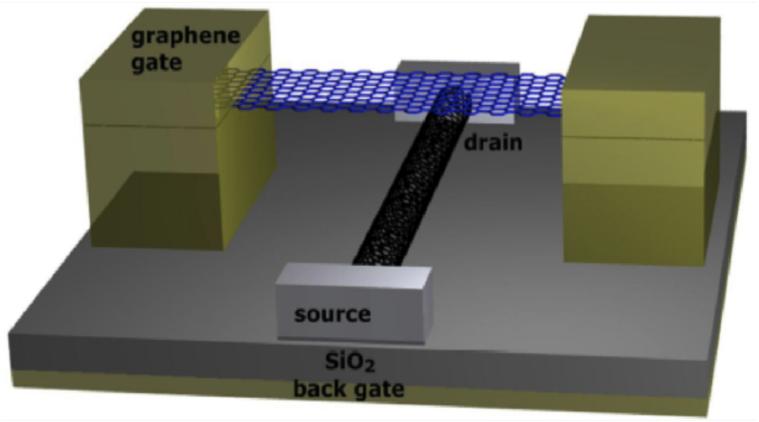

Figure 3.2: A Carbon NanoTube Field Effect Transistor (CNTFET) can be realised by adding to the prototypal NEMS structure a semiconducting nanotube. The graphene sheet is then used as a top gate. The flexibility of the top gate can be shown to enhance the switching of the transistor.

where C_{gg} (C_{bg}) is the graphene gate capacitance (backgate capacitance), V_{gg} (V_{bg}) is the graphene gate voltage (backgate voltage), $C_{\sum} = C_{gg} + C_{bg} + C_p$ where C_p is the parasitic capacitance and $\xi(Q)$ is the chemical potential of the CNT.

Since the switching of the transistor occurs when the charge of the nanotube is depleted, the above expression is analysed in the limit of very small accumulated charge on the CNT. In this limit, we find that

$$Q = Q_0 e^{(e\phi - E_0)/kT} \tag{3.17}$$

which is inverted to find the potential as a function of the charge,

$$\phi(Q) = \frac{kT}{e} \log\left(\frac{Q}{Q_0}\right) + E_0. \tag{3.18}$$

Inserting this into equation (3.16), we have in the limit $Q \ll Q_0$ that

$$\frac{kT}{e} \log\left(\frac{Q}{Q_0}\right) = \frac{V_{gg}C_{gg} + V_{bg}C_{bg}}{C_{\sum}}. \tag{3.19}$$

Assuming that the current is proportional to the carrier concentration, we find for the subthreshold slope,

$$S^{-1} = \frac{e}{kT \log(10)} \frac{\partial}{\partial V_{gg}} \left[\frac{C_{gg}V_{gg} + C_{bg}V_{bg}}{C_{\sum}}\right]. \tag{3.20}$$

Treating C_{gg} as a function of graphene voltage V_{gg}, this simplifies to

$$\frac{\log(10)kT}{e}S^{-1} = \frac{C_{gg}}{C_{\sum}}\left(1 + \frac{C'_{gg}C_{bg}}{C_{gg}C_{\sum}}\left(\Delta V + V_{gg}\frac{C_p}{C_{bg}}\right)\right), \tag{3.21}$$

where $\Delta V = V_{gg} - V_{bg}$ is the voltage difference between the graphene gate and the backgate, and $C'_{gg} = \frac{\partial C_{gg}}{\partial V_{gg}}$. The first term in the above expression gives the STS of the static gate transistor, while the second term summarises the effect of the non-static gate. First, we note that since the graphene gate capacitance C_{gg} will increase when the graphene sheet is deflected, the second term will always be positive, meaning that the subthreshold slope will always be larger for a non-static gate transistor as compared to a static gate transistor. Second, the first term is bounded by $\frac{C_{gg}}{C_{\sum}} < 1$. The case where $C_g = C_{\sum}$ is known as the thermal limit for the STS for a static transistor, giving a value of 60 mV/dec at room temperature. In the following, we will show that the moving gate transistor allows for STS even higher than this limit.

In paper I, (3.21) is analysed assuming a gate deflection on the form

$$u = u_1 \Delta V^{\alpha}, \tag{3.22}$$

where u_1 depends on the initial tension. For a completely linear graphene sheet, $\alpha = 2$ for deflections that are negligible compared to the distance between the graphene and the backgate. Mechanical nonlinearites cause α to decrease, so for small deflections we can assume $\alpha \lesssim 2$. Then,

$$C'_{gg} = \frac{\partial C_{gg}}{\partial u}\frac{\partial u}{\partial V_{gg}} = \frac{\alpha u}{\Delta V}\frac{\partial C_{gg}}{\partial u}. \tag{3.23}$$

From elementary electromagnetics we have for the capacitance per unit length between a cylinder and a plate

$$C = \frac{2\pi\epsilon}{\log\left(\frac{4h}{d}\right)}, \tag{3.24}$$

where h is the distance between the plate and the cylinder, d is the diameter of the cylinder, while ϵ is the dielectric constant of the surrounding medium. Thus the above relation is a function of the gate deflection u; however for a given geometry and back gate bias, the switching of the transistor will occur at a specific gate voltage, and hence at a specific gate deflection. To find this deflection, we note that at the switching, the following condition holds to a good approximation,

$$V_{gg}C_{gg} + V_{bg}C_{bg} = 0. \tag{3.25}$$

From this we infer that

$$\Delta V = \frac{|V_{bg}|(C_{gg} + C_{bg})}{C_{gg}}. \tag{3.26}$$

This analysis finally gives the following relation,

$$\frac{kT}{e}S^{-1} = \frac{C_{gg}}{C_{\sum}}\left(1 + \frac{C'_{gg}\Delta V}{C_{gg}\left(1 + C_{gg}/C_{bg}\right)}\right). \tag{3.27}$$

Now, using equation (3.24) and (3.22) we can rewrite this as

$$\frac{kT}{e}S^{-1} = \frac{C_{gg}}{C_{\sum}}\left(1 + \frac{C_{gg}\alpha u}{2\pi\epsilon(h-u)(1 + C_{gg}/C_{bg})}\right), \tag{3.28}$$

where h is the suspension height of the graphene sheet over the CNT. This analysis leaves two fitting parameters; the parasitic capacitance C_p and the parameter u_1. In figure(3.3), STS is plotted for some different values of u_1 as a function of suspension height. The experimentally obtained point is marked with a dot. The horizontal dashed line is the thermal limit of S^{-1}. We note that the suspension height necessary for beating the thermal limit increases with increasing values of u_1 (equivalent to decreasing T_0). The dashed curve is the subthreshold slope in the limit of infinite initial tension in the graphene, corresponding to a static graphene gate. Also included in the figure are iso-deflection curves; i.e curves which obey $\frac{\partial S}{\partial(u/h)} = 0$. The intersection of these dotted curves with the inverse S curves gives the ratio of the deflection of the suspended graphene with the distance between graphene and CNT. What we infer from this is that at the thermal limit, the graphene sheet will have a very large deflection, typically more than 80% of the graphene-CNT distance. However, as derived in the previous section, when the graphene deflects more than roughly 60% of the graphene-CNT distance, the electrostatic forces will overcome the elastic forces acting on the graphene sheet, and the graphene will snap-in to the dielectric, rendering the device useless. Following the 60% iso-deflection curve we find that to beat the thermal limit before snapping in to the surface at the experimental level of parasitic capacitance, a static

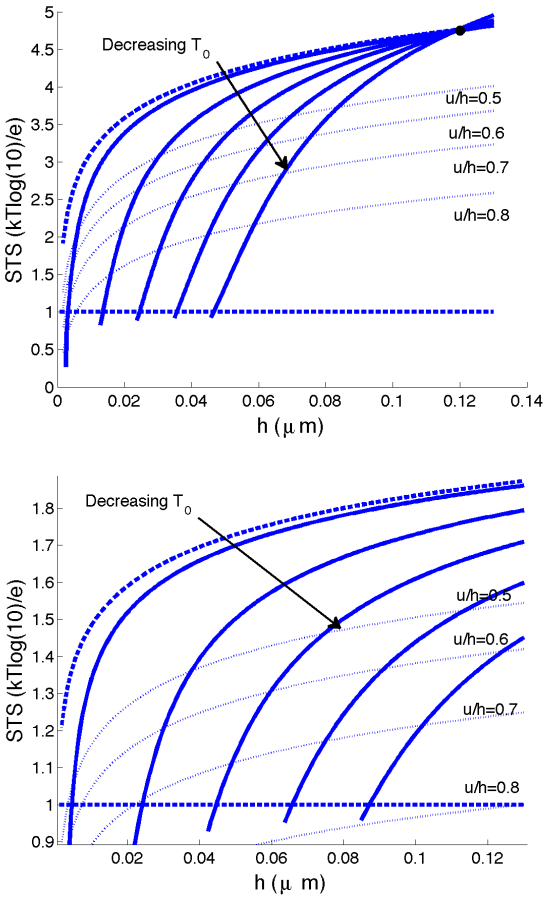

Figure 3.3: The subthreshold slope as a function of the CNT-Graphene gate distance, for various values of u_1. Upper figure: With parasitic capacitances fitted to the experimental data. In order to avoid snap-in at the thermal limit, the suspension height cannot be larger than 3 nm. Lower figure: Without inclusion of parasitic capacitance. Now, the suspension height can be ~ 10 nm without snapping in at the thermal limit.

graphene-CNT distance of a mere 3 nm would be required, and an initial tension of the graphene $T_0/T_1 \approx 0.45\%$.

Removing the parasitic capacitance completely slightly alleviates the requirement on the suspension height, although the suspension height still needs to be < 20 nm to beat the thermal limit.

It is worth noting that this analysis does not take into account that close to the snap-in instability, the derivative of the graphene-nanotube capacitance, C_{gg}, grows rapidly. As a consequence, the subthreshold slope will always tend to zero at the snap-in. However, utilising this particular effect in an actual transistor is not very realistic, since the snap-in instability is irreversible. Once the graphene snaps into the subrate, it is stuck. Therefore, it is not expected that solving the full equation for the static deformation of the graphene will give any considerable contributions to the analysis.

We note as a general feature of this kind of system, there is a balance between wanting the graphene sheet to respond heavily to an applied voltage, and at the same time avoiding snap-in to the subrate. This balance is reflected in the existance of an optimal value of the parameter T_0: increasing the initial tension from this value, the suspension height required to reach the thermal limit will increase. Decreasing the inital tension, the sheet will always snap-in to the substrate before reaching the thermal limit.

Chapter 4

Modes of dissipation in suspended graphene resonators

The elastodynamic considerations of the preceding section did not adress the issue of dissipation. This is often accounted for by including a phenomenological damping coeffiecient in the equations of motion. While this procedure is sufficient for most modelling purposes, in order to give quantitative predictions on the impact of dissipation in a system, a more fundamental microscopic model is needed.

In the past, several modes of dissipation have been investigated [22, 23, 24, 25]. In general, dissipation can be described through the interaction of the system with an external bath of oscillators.

The interaction allows for energy to be transferred between the system and the bath. The same process that is responsible for transferring energy from the system to the bath, will also result in thermal fluctuations in the bath that transfer energy to the system. In thermal equilibrium, the rate of energy transfer from the system to the bath and from the bath to the system must be equal. There is no net energy flow. This gives a relation between the thermal fluctuations and the dissipation in a system. This notion is formalised in the *fluctuation-dissipation theorem* [26].

It is important to note that if energy is transferred to the system externally, i.e. if the system is driven by some external force, there is no need for the system and the bath to be in thermal equilibrium. Then, energy may be transferred from the system to the bath at a higher rate than from the bath to the system.

In an ongoing project, the system is taken to be the out-of-plane motion of the graphene, while the bath is the in-plane motion of the graphene coupled to the phononic bath in the substrate beneath the graphene. The coupling between the out-of-plane motion and the in-plane motion give rise to dissipation, as is shown in the subsequent section.

4.1 Damping due to mechanical nonlinearities

Consider an infinite graphene sheet, free to displace vertically in a region of length l, otherwise perfectly clamped vertically (see figure 4.1). The in-plane motion of the sheet is coupled harmonically to a substrate with coupling parameter Λ. The graphene is treated as a quasi-1D structure, i.e. the graphene is assumed to be static in the y-direction. In that case, the elastic free energy density of the graphene in the membrane approximation defined in chapter 2 is given by (2.7)

$$F = T_0 w_x^2 + \frac{T_1}{2}\left(u_x^2 + u_x w_x^2 + w_x^4/4\right) + \frac{\Lambda(x)}{2}\left(u - s_\Omega\right)^2 + f(x,t)w. \tag{4.1}$$

where $T_1 = 2\mu + \lambda$ is a linear combination of the Lamé parameters, T_0 is the initial tension of the graphene, s_Ω is the displacement field in x-direction at the surface of the substrate and $f(x,t)$ is an externally applied pressure. The spatial dependence of the coupling constant reflects that the coupling vanishes in the suspended region.

It is worth noticing that in this model, the graphene is attached to a three-dimensional elastic medium. The medium extends throughout the entire half-space beneath the sheet. This will over-estimate the rigidity of the substrate.

From the Euler-Lagrange equations the following equations of motion for the in-plane and out-of-plane motion are derived,

$$\begin{aligned} \rho_G \ddot{u} - T_1 u_{xx} &= \frac{T_1}{2}\partial_x\left(w_x^2\right) + \Lambda(x)(u - s_\Omega) \\ \rho_G \ddot{w} &= T_0 w_{xx} + \frac{T_1}{2}\partial_x\left[\left(2u_x + w_x^2\right)w_x\right] + f(x,t). \end{aligned} \tag{4.2}$$

Writing $w(x,t) = q(t)\phi(x)$ where $\phi(x)$ has support only in the suspended region and $\int_{-l/2}^{l/2}\phi(x)^2 = l$ where l is the length of the suspended region and

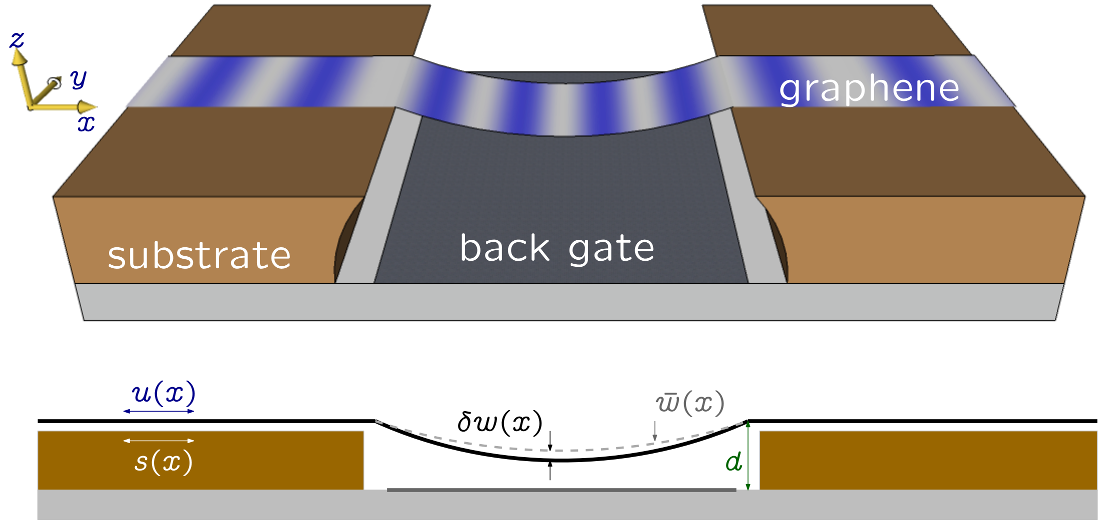

Figure 4.1: Schematic image of a suspended graphene sheet. Note that in the model used in this thesis, the trench enters only as a region of vanishing coupling between the graphene and the underlying substrate

writing $f(x,t) = f_0 \cos(\omega t)$, the last of these equations transforms to

$$\ddot{q} + \omega_0^2 q + \alpha_0 q^3 + \frac{T_1}{\rho_G l} q \langle u_x \phi_x^2 \rangle = \frac{f_0 \cos(\omega t)}{\rho_G l} \langle \phi \rangle \tag{4.3}$$

where $\langle fg \rangle$ is shorthand for $\int_{-l/2}^{l/2} dx f(x) g(x)^*$, and ω_0 and α_0 are the resonance frequency and the Duffing parameter, respectively, as given in chapter 2. The effect of coupling to the in-plane motion is completely contained in the overlap $\langle u_x \phi_x^2 \rangle$. To find this overlap integral, we turn to the in-plane motion.

Since the coupling parameter $\Lambda(x)$ has support only in the nonsuspended part of the graphene, the equation of motion for the in-plane motion in the suspended region is

$$\ddot{u} - \frac{T_1}{\rho_G} u_{xx} = \frac{T_1}{2\rho_G} q(t)^2 \partial_x \left(\phi_x^2 \right). \tag{4.4}$$

Note that this is the wave equation with a source term $\frac{T_1}{2} \partial_x \left(w_x^2 \right)$. The in-plane motion can therefore be written in terms of a response function,

$$u(x,t) = \frac{T_1}{2\rho_G} \int dx' dt' R(x, x', t-t') q(t')^2 \partial_x \left(\phi_x(x',t')^2 \right) \tag{4.5}$$

The form of the response function $R(x, x', t - t')$ is determined by the interaction with the substrate. For external forces that are periodic with frequencies ω close to ω_0, the response of the out-of-plane amplitude is written as

$$q(t) = q_0 + \frac{1}{2}\left(q_1(t)e^{i\omega t} + q_1(t)^* e^{-i\omega t}\right); \quad \dot{q} = \frac{i\omega}{2}\left(q_1(t)e^{i\omega t} - q_1(t)^* e^{-i\omega t}\right) \tag{4.6}$$

where q_0 is the static response and q_1 is a slowly varying function of time. At this point, it is worth considering the length and time scales involved in the problem. Disregarding the graphene-substrate coupling for a moment, the wavelength of the emitted in-plane phonons will be $\lambda \sim \frac{c_G}{2\pi\omega} = l\sqrt{\frac{T_1}{T_0}}$, where $c_G \equiv \sqrt{T_1/\rho_G}$ is the sound velocity of graphene. Since $\frac{T_1}{T_0} \sim 10^{-3}$ for typical graphene sheets fabricated by exfoliation, the phonon wavelength will be of the order $10 - 100\mu$m for a suspension length of 1μm, which is typically larger than the entire graphene sheet. The propagation time for such a phonon across the suspended region is similarly much shorter than the period of oscillation for the out-of-plane motion. Then, the slowly varying q_1 can be pulled out of the time integral, resulting in

$$\begin{aligned} u(x,t) =& \frac{c_G^2}{2}\left[\left((q_0^2 + \frac{|q_1|^2}{2}\right)\int dx'dt' R(x, x', t-t')\partial_x\left(\phi_x(x')^2\right) + \right. \\ & q_0 q_1 e^{i\omega t}\int dx'dt' R(x, x', t-t') e^{i\omega(t'-t)}\partial_x\left(\phi_x(x')^2\right) + \\ & \left.\frac{q_1^2}{4}e^{2i\omega t}\int dx'dt' R(x, x', t-t') e^{2i\omega(t'-t)}\partial_x\left(\phi_x(x')^2\right)\right] + c.c. \end{aligned} \tag{4.7}$$

Note that the time integrals in the expression above can be expressed as Fourier transforms of the response function $\tilde{R}(x, x', \Omega)$. Each of the integrals correspond to a specific frequency component of the in-plane motion. Writing $u(x,t) = u_0 + \frac{1}{2}\left(u_\omega(x,t)e^{i\omega t} + u_\omega^*(x,t)e^{-i\omega t}\right) + \frac{1}{2}\left(u_{2\omega}(x,t)e^{2i\omega t} + u_{2\omega}^*(x,t)e^{-2i\omega t}\right)$ these different components are given by

$$\begin{aligned} u_0(x,t) =& \frac{c_G^2}{2}\left(q_0^2 + \frac{|q_1|^2}{2}\right)\varphi(x,0) \\ u_\omega(x,t) =& c_G^2 q_0 q_1(t)\varphi(x,-\omega) \\ u_{2\omega}(x,t) =& c_G^2 \frac{q_1^2(t)}{4}\varphi(x,-2\omega), \end{aligned} \tag{4.8}$$

where $\varphi(x,-\Omega) \equiv \int dx' \tilde{R}(x,x',-\Omega)\partial_x\left(\phi_x(x')^2\right)$. Inserting these expressions into the equation for the out-of-plane motion and averaging the equation over one period, the equation becomes,

$$
\begin{aligned}
i\omega\dot{q}_1 + \frac{1}{2}\left(\omega_0^2 - \omega^2 + 3\alpha q_0^2\right)q_1 + \frac{3}{8}\alpha_0|q_1|^2 q_1 + \frac{c_G^4}{2l}q_0^2 q_1\langle\varphi_x(x,-\omega)\phi_x^2\rangle + \\
\frac{c_G^4}{4l}q_1\left(q_0^2 + \frac{|q_1|^2}{2}\right)\langle\varphi_x(x,0)\phi_x^2\rangle + \\
\frac{c_G^4}{4l}\frac{|q_1|^2 q_1}{4}\langle\varphi_x(x,-2\omega)\phi_x^2\rangle = \frac{f_0}{2\rho_G l}\langle\phi\rangle. \qquad (4.9)
\end{aligned}
$$

Depending on the form of the response function $R(x,x',t-t')$, the overlap integrals will have both real and imaginary parts. The real parts will renormalise the resonance frequency and Duffing parameter, while the imaginary parts correspond to dissipation. The term containing $\varphi(x,\omega)$ is linear in the out-of-plane amplitude, and corresponds to a linear viscous damping. On the other hand, the term containing $\varphi(x,2\omega)$ multiplies $q_1|q_1|^2$ and corresponds to an amplitude dependent, or nonlinear, damping. The importance of this damping is determined partly by the ratio between the nonlinear damping and the linear damping, and partly by the ratio between the nonlinear damping and the Duffing parameter. To separate the terms, the following notation is introduced,

$$
\begin{aligned}
\gamma =& \frac{c_G^4}{l}q_0^2\mathrm{Im}\{\langle\varphi_\mathrm{x}(\mathrm{x},-\omega)\phi_\mathrm{x}^2\rangle\} \\
\eta =& \frac{c_G^4}{2l}\mathrm{Im}\{\langle\varphi_\mathrm{x}(\mathrm{x},-2\omega)\phi_\mathrm{x}^2\rangle\} \\
\frac{3}{8}\tilde{\alpha} =& \frac{3}{8}\alpha + \frac{c_G^4}{8l}\mathrm{Re}\left\{2\langle\varphi_x(x,0)\phi_x^2\rangle + \langle\varphi_x(x,-2\omega)\phi_x^2\rangle\right\} \\
\tilde{\omega}_0^2 =& \omega_0^2 + \left(3\alpha + \frac{c_G^4}{4l}\langle\varphi_x(x,0)\phi_x^2\rangle + \frac{c_G^4}{2l}\mathrm{Re}\left\{\langle\varphi_x(x,-\omega)\phi_x^2\rangle\right\}\right)q_0^2. \qquad (4.10)
\end{aligned}
$$

The equation of motion can then be written

$$
i\omega\dot{q}_1 + \frac{1}{2}\left(\tilde{\omega}_0^2 - \omega^2\right)q_1 + \frac{3}{8}\tilde{\alpha}|q_1|^2 q_1 + i\frac{1}{2}\gamma q_1 + i\frac{1}{8}\eta|q_1|^2 q_1 = \frac{f_0}{2\rho_G l}\langle\phi\rangle. \qquad (4.11)
$$

Following Dykman [27], the following dimensionless quantities are investigated,

$$\begin{aligned}\delta =&\frac{\eta|q_1|^2}{4\gamma} = \frac{\mathrm{Im}\left\{\langle\varphi_x(x,-2\omega)\phi_x^2\rangle\right\}|q_1|^2}{\mathrm{Im}\left\{\langle\varphi_x(x,-\omega)\phi_x^2\rangle\right\}q_0^2}\\ \tilde{\eta} =&\frac{\eta\omega}{\tilde{\alpha}}.\end{aligned} \tag{4.12}$$

The first of the dimensionless quantities measures the relative magnitude of the linear and nonlinear damping. This is determined by the ratio of the overlap integrals, which is a purely geometrical quantity, and the ratio between the vibrational amplitude and the static deformation of the graphene sheet. For a small static deformation, it is therefore expected that the nonlinear damping dominates the dissipation caused by this mechanism. The second quantity measures the relative importance of the two nonlinearities in the equation. For $\eta < \sqrt{3}$, the well-known bifurcation of the Duffing equation is present, while for $\eta > \sqrt{3}$ this bifurcation vanishes [27]. This is a purely geometrical factor, apart from the weak dependence of ω on the static deformation of the graphene.

As a measure of the total dissipation due to this mechanism, we consider the quality factor, defined as

$$Q = \frac{\omega\bar{E}}{\dot{\bar{E}}}, \tag{4.13}$$

where $\bar{E}$ is the energy of the subsystem of interest, averaged over one period. Here, the concern is the damping of the out-of-plane motion. The energy E is consequently the part of the energy of the graphene related to the out-of-plane motion,

$$E = \rho\frac{\dot{w}^2}{2} + T_0 w_x^2 + \frac{T_1}{2}\left(u_x w_x^2 + \frac{w_x^4}{4}\right). \tag{4.14}$$

Inserting the expressions for u and w derived above and performing the averaging, the expression for the quality factor becomes

$$Q^{-1} = \frac{4\gamma + \eta|q_1|^2}{4\left(\omega^2 + \frac{3}{16}\alpha|q_1|^2\right)} \tag{4.15}$$

To evaluate these dimensionless quantities, we need to consider the coupling to the substrate explicitly. The equation for the substrate will be [28]

$$\rho_{\mathrm{S}}\frac{\partial^2}{\partial t^2}\vec{s} = \mu\vec{\nabla}^2\vec{s} + (\mu+\lambda)\vec{\nabla}\vec{\nabla}\vec{s} = 0 \tag{4.16}$$

The boundary condition is that the stress at the surface of the substrate must compensate for the stress induces by the in-plane motion of the graphene,

$$\sigma_{xz}|_{z=0} = \Lambda\left(u - s_\Omega\right). \tag{4.17}$$

Since the equation for the substrate is linear, the response of the substrate at the surface can be given in terms of a linear response function M_{xx},

$$s_\Omega(\vec{x}, z=0, \omega) = -\int d^2x' M_{xx}(\vec{x}-\vec{x}', \omega)\sigma_{xz}\left(\vec{x}', z=0, \omega\right) . \tag{4.18}$$

In a quasi-1D geometry, the y-integration can be performed as a partial Fourier transform, resulting in

$$s_\Omega(x, k_y, z=0, \omega) = -\int dx' M_{xx}(x-x', k_y, \omega)\Lambda(x')\left(u(x', \omega) - s_\Omega(x', k_y, \omega)\right), \tag{4.19}$$

where σ_{xz} is replaced by $\Lambda(x)\left(u(x,\omega) - s_\Omega\left(x', k_y, \omega\right)\right.$. It is sufficient to consider $k_y = 0$, so this will be supressed in the following. Discretising the graphene sheet in the x-direction, this can be written as

$$\begin{aligned} s_\Omega(x_j) &= -\sum_i \int_{x_i-h/2}^{x_i+h/2} dx' M_{xx}(x_j - x', \omega)\Lambda(x_i)(u(x_i,\omega) - s_\omega(x_i,\omega)) \\ &\equiv -\sum_i R_{ij}(\omega)\Lambda(x_i)(u(x_i,\omega) - s_\omega(x_i,\omega)) \end{aligned} \tag{4.20}$$

This is still an implicit expression for s_Ω. Introducing the matrices $\mathbb{R}$ and $\mathbb{K}$ with components $R_{ji}(\omega)$and $K_{ji}(\omega) = \Lambda(x_i)(\omega)\delta_{ij}$ and rearranging, one finds

$$\mathbb{K}\left(\mathbf{u} - \mathbf{s}\right) = \left[\mathbb{I} - \mathbb{K}\mathbb{R}\right]^{-1}\mathbb{K}\mathbf{u} \tag{4.21}$$

This result is inserted into the equation for the in-plane motion of the graphene,

$$-\omega^2\mathbf{u} - c^2\mathbb{L}\mathbf{u} + \frac{1}{\rho}\left[\mathbb{I} - \mathbb{K}\mathbb{R}\right]^{-1}\mathbb{K}\mathbf{u} = \mathbf{F}(\omega) , \tag{4.22}$$

where $\mathbf{F}$ represents the discretised and Fourier transformed source term of (4.2), and $\mathbb{L}$ is the discretised version of the second derivative operator. Taking the response function from [29, 30],

$$\begin{aligned}
M_{xx}(k_x,k_y,\omega) =& -\frac{i}{\rho_S c_T^2 k^2}\left[\frac{\mathrm{p}_2(\omega,k)k_x^2}{\left(\omega^2/c_T^2-2k^2\right)^2+4k^2\mathrm{p}_1(\omega,k)\mathrm{p}_2(\omega,k)}+\frac{k_y^2}{\mathrm{p}_2(\omega,k)}\right];\\
\mathrm{p}_1(\omega,k) =& \mathrm{sign}(\omega)\sqrt{\frac{\omega^2}{c_L^2}+\mathrm{sign}(\omega)i\epsilon-k^2}\\
\mathrm{p}_2(\omega,k) =& \mathrm{sign}(\omega)\sqrt{\frac{\omega^2}{c_T^2}+\mathrm{sign}(\omega)i\epsilon-k^2},
\end{aligned} \tag{4.23}$$

where c_T and c_L are the transverse and longitudinal sound velocities of the substrate, this equation is solved numerically.

To evaluate the quality factor, the static displacement and the amplitude of vibrations must also be calculated. The out-of-plane motion is projected onto the fundamental mode of the resonator, $\phi(x)=\sqrt{2}\cos\left(\frac{\pi x}{l}\right)$. The static displacement q_0 is calculated as a function of the applied static bias voltage V_{dc} in the same approximation as in chapter 3, assuming a parallel plate capacitance between the back gate and the graphene. The response of the substrate is ignored in this approximation. The static displacement is then given by

$$q_0=\sqrt{2}\frac{\epsilon l^2 V_{dc}^2}{\pi^3 T_0 d^2} \tag{4.24}$$

To find the amplitude of the vibrational motion, the following dimensionless variables

$$\tilde{f}=\frac{f}{\omega^3}\sqrt{\frac{\alpha}{\rho_G^2}};\quad |\tilde{q}_1|=q_1\sqrt{\frac{\alpha}{\omega^2}} \tag{4.25}$$

are introduced, where f is the amplitude of the oscillating force, projected onto the fundamental mode shape. Then, following [31], the amplitude of the vibrational motion of the Duffing oscillator is given by the relation

$$\tilde{f}=|\tilde{q}_1|\left(4\gamma/\omega+|\tilde{q}_1|^2\right) \tag{4.26}$$

This analysis enables the calculation of η, γ and Q. In the following, a graphene sheet of suspended length 1 μm and initial tension $T_0=0.34$ N/m$=10^{-3}T_1$ on top of a SiO$_2$ substrate is considered. The coupling parameter Λ is taken from the literature to be $\Lambda=10^{20}$ N/m^3 [32], and the distance to the back-gate is $d=330$nm. Furthermore, the total length of the graphene sheet

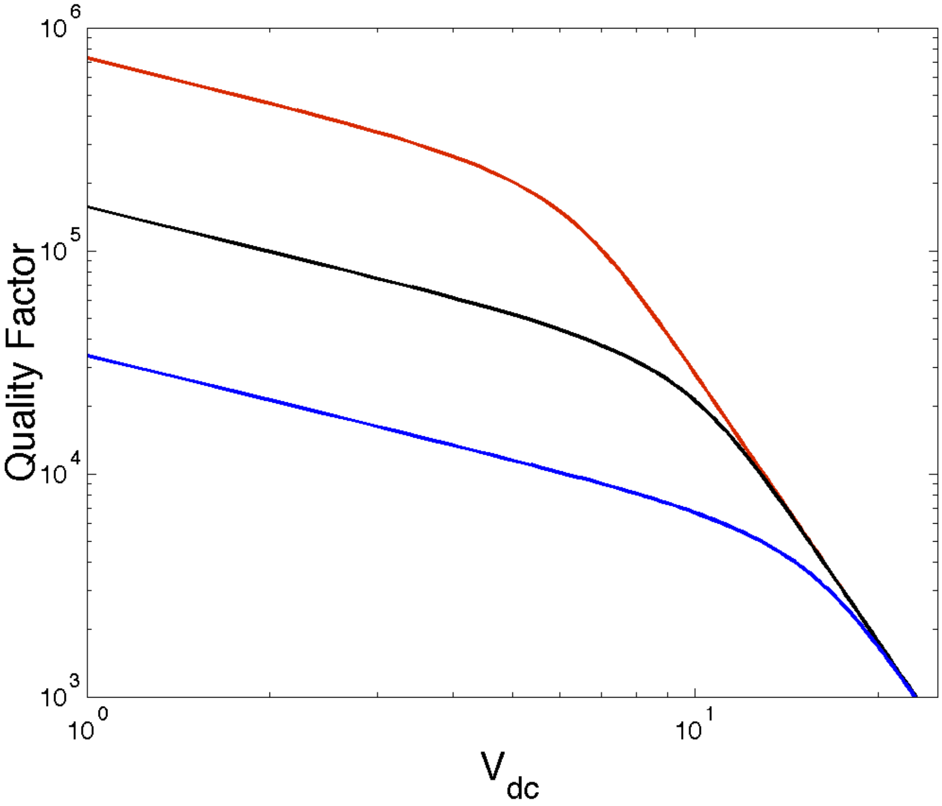

Figure 4.2: The quality factor Q as a function of bias voltage V_{dc}. The quality factor is evaluated for $V_{ac} = 10\mu$V (blue line), $V_{ac} = 100\mu$V (black line) and $V_{ac} = 1$mV (green line).

is taken to be 3μm. For this particular geometry, the values $\tilde{\eta} = 0.19$ and $\delta = 0.42$ is obtained. Thus, nonlinear damping is not strong enough to obliterate the Duffing bistability. In fact, $\tilde{\eta} < \sqrt{3}$ in all conducted simulations.

In figure 4.2, the quality factor Q is plotted as a function of V_{dc} for three values of the driving voltage V_{ac} at the vibrational resonance of the graphene resonator. There is a clear kink in the quality factor, signifying the transition from nonlinear to linear damping dominated regimes. The dependence of the quality factor on the bias voltage is qualitatively different in the two regimes, something that could be used for experimental verification of nonlinear damping. Another signifying feature of the nonlinear damping regime is that the quality factor in this regime depends on the alternating voltage, while it is independent of alternating voltage in the linear regime.

For this particular geometry, the nonlinear damping will dominate for bias voltages $V_{dc} \lesssim 10$ V. The resulting quality factor lies in the range 10^4-10^6, similar in magnitude to those reported in experiments of $Q \sim 10^5$ [18]. The coupling between the flexural motion of the graphene sheet and the in-plane motion may therefore be a contributing mechanism for dissipation, and may give rise to measurable nonlinear dissipation for small bias voltages. However, this mechanism alone will not remove the Duffing bistability.

Chapter 5

Bending rigidity of graphene

In all previous models in this thesis, the energy cost of bending the graphene sheet has been disregarded. This is often a valid approximation, particularly when the sheet is under tension. At Gothenburg University, devices have been fabricated where *compressive* strain is used to engineer the shape of the suspended graphene sheet. The compressive strain is achieved through thermal cycling before making the graphene suspended. After making the graphene suspended, the compressive strain is released and the graphene buckles. The interaction with the electrodes breaks the spatial symmetry of the buckling, causing the graphene to buckle toward the electrodes. This way, the graphene buckles can be assessed electrostatically (figure 5.1). In these prebuckled structures, the response to an applied pressure is determined by the relative balance between bending and stretching energy. As a consequence, the bending rigidity of the graphene can no longer be neglected. Since the bending rigidity has a very limited effect on the mechanical properties of graphene in most structures, the numerical value of this parameter is much less established than the elastic stiffness of graphene. In the present case, the response of the sheet will be determined by the relative balance of the elastic stiffness and bending rigidity. Hence, these structures give us a unique opportunity to measure the bending rigidity directly. Before describing the details of the measurements, I give a brief review on the current status of the bending rigidity of graphene.

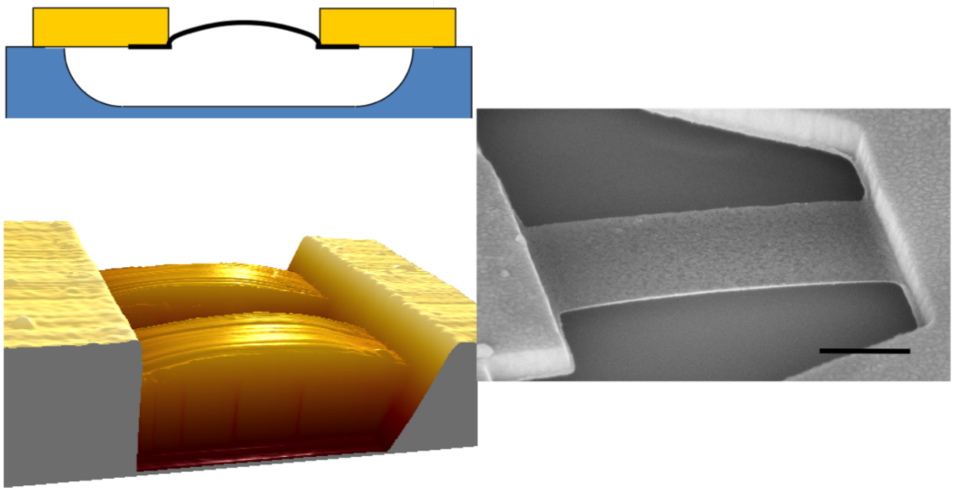

Figure 5.1: Visualisation of the buckled structures. The upper image is a schematic image of the resulting structure. Beneath it to the left is an AFM image of an experimental structure, and to the right an STM image. In both images the resulting curvature is clearly visible.

5.1 Bending rigidity of graphene: current status

The bending rigidity of bulk elastic materials is due to the stretching and compression in different parts of the material as a consequence of the bending deformation. The bending rigidity of such materials scale with thickness and Young's modulus as $\kappa \sim Eh^3$. For monolayer graphene, this tension-compression model of bending stiffness does not apply, since graphene is two dimensional. The bending rigidity must therefore have a different origin.

One such origin is the change in bond angles in the hexagonal atomic structure associated with changing the curvature of the graphene sheet. This effect can be estimated using so called bond order potentials, an empirical set of potentials designed to describe the energetics of molecular bonds. Estimates based on bond order potentials as well as ab initio calculations give values of $\kappa \sim 1$eV [33, 34, 35]

It is worth noting, that this estimate is given in the limit of zero temperature. At higher temperatures, thermal fluctuations causes ripples in the graphene sheet that are approximately 80Åwide that screens long wavelength deformations such as bending. The bending rigidity is consequently increased to about $\sim 2eV$ at $T = 3500K$ [36].

Admittedly, this predicted increase in bending rigidity by a factor of two when increasing the temperature from 0 K to 3500 K does not imply a dramatic thermal effect. The case is quite different, in fact, when moving from a single graphene layer to a bilayer [37]. At low temperatures the two layers will follow each other rigidly, reinstating the tension-compression model as the primary origin of bending stiffness already for membranes only two atoms thick. The bending rigidity here is easily estimated considering two thin plates separated by a distance h. When deforming this system, we consider a hypothetical neutral surface between the thin plates that is not stretched. If the system is bent into a cylinder with radius of curvature R at the neutral surface, the radii of curvatures of the two plates become $R + h/2$ and $R - h/2$ respectively. Compared to the nonstretched neutral surface, the relative tension/compression of an infinitesimal length element on each of the plates is consequently given by $h/2R$. The energy associated with this deformation is $\Delta E = \frac{T_1}{2}\left(\frac{h}{2R}\right)^2$ for each plate, where $T_1 = \lambda + 2\mu$. The bending rigidity is the parameter in the free energy multiplying the inverse radius of curvature squared. Thus, $\kappa = T_1\frac{h^2}{4}$. Using $T_1 = 340$ N/m [38] and $h = 3.4$Å, this evaluates to $\kappa \sim 160$ eV. This naive estimate is in excellent agreement with ab initio calculations using bond order potentials, giving values ranging from 160 to 180 eV [34] at $T = 0$ K. Thus, the energy of bending a bilayered graphene sheet at low temperatures mainly comes from the tension-compression energy, indicating that elasticity theory again prevails.

If, however, the temperature is increased from $T = 0$ K, the individual graphene layers will create the same kind of thermal ripples described above. At short distances, the graphene layers will appear to move independently, meaning that the bending rigidity on this length scale (~ 80 Å) is drastically reduced to that of two monolayer graphene sheets, i.e. $2 - 4$ eV. At the same time, the graphene sheets appear to conserve stacking order despite the rippling. On longer length scales the sheets therefore do not move independently, and a significantly larger bending rigidity is expected. Thus, the issue of bending rigidity of bilayered graphene on experimentally relevant length scales is far more involved than its monolayered counterpart and experimental determination of this parameter, both for monolayered and few-layered graphene, is of significant importance for our understanding of the microscopic behaviour of graphene.

5.2 Measuring the bending rigidity

As mentioned previously, the energy cost of bending a graphene sheet is extremely small compared to the energy required to stretch the sheet, so small that the former is typically neglected completely compared to the latter when modeling the mechanics of flat suspended graphene. It is therefore very difficult to experimentally estimate the value of this parameter by directly investigating the mechanical response of the graphene. In fact, the only reported experimental estimate of the bending rigidity of monolayered graphene comes from studies of the phonon spectrum of graphite [39], giving values consistent with ab initio calculations. On the other hand, nano-indentation measurements have proven successful for determining the bending rigidity of thicker flakes (more than 8 layers) [40] where the difference in energy scales between bending and stretching is less pronounced.

In the measurement scheme developed by our group in collaboration with an experimental group at Gothenburg University, the inherent difficulties in measuring the bending rigidity are avoided by tuning the geometry to our advantage. Through thermal cycling a compressive strain is built up within the graphene sheet, which is released when the sheet is suspended causing the sheet to buckle (figure 5.2). When an external pressure is applied to these prebuckled structures, the resulting deformation is small until a critical pressure is reached, where the structures display a snap-through instability. This instability is probed by gradually increasing the voltage on the back gate while keeping an AFM tip in tapping mode on the graphene structure. The sudden change in height on the AFM is a signature of the snap through. A typical structure with snap through instability is shown in figure 5.2. A schematic image of the process of snap through is seen in figure 5.4.

The instability was observed also in fully clamped structures, depicted in figure 5.3. For fully clamped structures, continuum elasticity theory gives an expression for the critical pressure,

$$p_c = \frac{4\sqrt{\kappa n T_1}}{R_1 R_2} \tag{5.1}$$

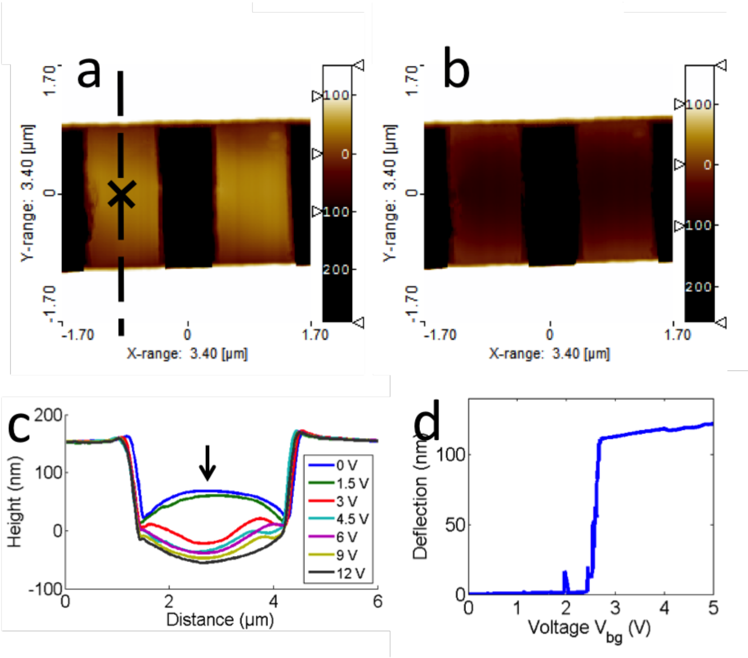

Figure 5.2: A doubly clamped structure showing a snap through instability. a) and b) are AFM images of the sample at 0V and 3V, respectively. In c), AFM sweeps have been made along the dashed line in a) while gradually increasing the voltage. In d) the AFM tip is kept fixed at the spot marked with a cross in a) while gradually increasing the voltage. Here, the snap-through instability manifests itself as the discontinuity in tip position at 2.6V.

where n is the number of graphene layers and R_1 and R_2 are the principal radii of curvature. It is worth noting that the instability requires curvature in two directions, or equivalently a nonvanishing Gaussian curvature. This is due to a result from differential geometry, stating that pure bending can occur only in surfaces with a vanishing Gaussian curvature. Thus, to obtain the desired competition between bending and stretching, one needs curvature in two directions. Since the bending rigidity is very small for graphene membranes, a sheet with vanishing Gaussian curvature will respond heavily to an applied pressure through pure bending. The detailed calculation leading up to equation (5.1) is far too involved to be included in this thesis; the reader is here referred to Pogorelov [41]. The scaling of the critical pressure can

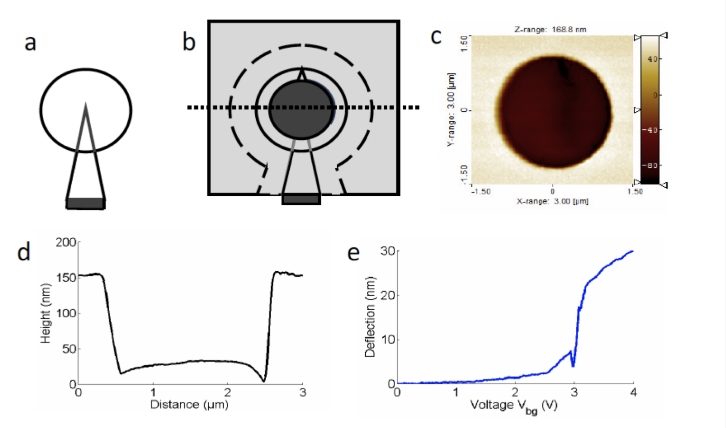

Figure 5.3: A fully clamped structure showing a snap through instability. a) and b) are AFM images of the sample at 0V and 3V, respectively. In c), AFM sweeps have been made along the dashed line in a) while gradually increasing the voltage. In d) the AFM tip is kept fixed at the spot marked with a cross in a) while gradually increasing the voltage. Here, the snap-through instability manifests itself as the discontinuity in tip position at 3V.

however be found from rather simple considerations.

Assume that a small pressure, well below the critical pressure, is applied to a shallow spherical shell of radius R. The shell will respond by locally becoming "flatter" at the top of the shell. In other words, in a region of width d, the radius of curvature increases from R to $R' > R$ (figure 5.5). As the radius of curvature R' increases, the graphene within the flattened region is compressed. At some pressure, the deformed part of the shell will be completely flat. Deforming the shell further, the compressive strain will be released until the deformed part of the shell form a mirror image of its original shape. Then, both the bending and stretching contributions to the energy will be equal to the undeformed shell, apart from a considerable bending in a region close to the edge of the deformed region. In other words, the deformation of a shallow shell will be qualitatively different for small and large applied pressures. It turns out that the latter configuration is unstable under an applied pressure. The pressure at which the transition between the two types of deformation occurs will therefore be the critical pressure.

The deformation at small pressures is parametrised by the width and depth of the deformation according to figure 5.5). We aim at finding these parameters by minimising the free energy of the system.

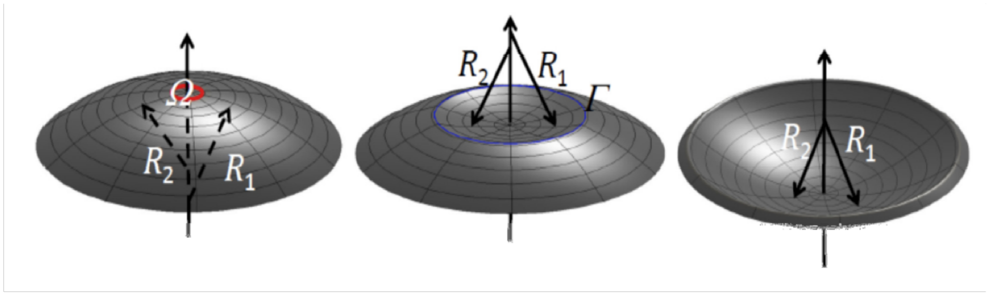

Figure 5.4: A schematic view of the process of snap through. Left: For small pressures a local deformation is formed in the region denoted Ω.Middle: When the critical pressure is reached, it becomes energetically favourable to form a concave region where the elastic energy is confined to a narrow region Γ. Right: This concave region is elastically unstable. As a result, the deformation propagates outward, and the sheet snaps through.

The elastic energy is divided into two parts, $U_{tot} = U_b + U_s$. The bending energy density is given by

$$u_b \sim \kappa(\xi'')^2, \tag{5.2}$$

where ξ is the deflection of the shell in the radial direction, and the differentiation is with respect to a length element ds in the meridial direction. Since the deflection changes by H over a distance d, the second derivative can be approximated by

$$\xi'' \sim \frac{H}{d^2}. \tag{5.3}$$

The bending energy density thus becomes

$$u_b \sim \kappa\frac{H^2}{d^4}. \tag{5.4}$$

As for the stretching energy density, it is given by

$$u_s \sim T\epsilon^2, \tag{5.5}$$

where ϵ is the strain. For a spherical shell, the relative elongation of the equator due to a homogeneous radial displacement ξ is $\frac{2\pi\xi}{2\pi R} = \frac{\xi}{R}$. Hence, the strain is $\epsilon = \frac{\xi}{R} \sim \frac{H}{R}$,

$$u_s \sim T\frac{H^2}{R^2}. \tag{5.6}$$

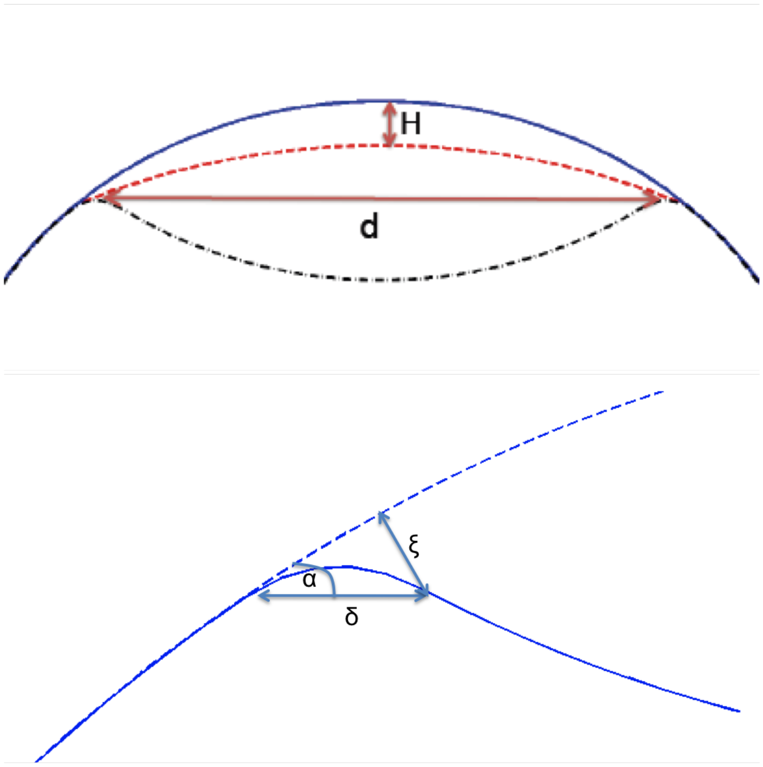

Figure 5.5: Top: Shells under external pressure display two qualitatievely different regions of deformation, indicated in the figure by the dashed and dash-dotted line. At low pressures, the shell will locally flatten, decreasing the local curvature. For large pressures, the deformed part of the shell will form a mirror image of its undeformed counterpart. The main contribution to the elastic energy will then be contained in a narrow region close to the edge of the deformed region. Bottom: Close-up of the edge of the deformation for large pressures. The edge region can be parametrised by a width δ and an angle α.

The total elastic energy is the energy density times the area of the bulge, which scales as d^2,

$$U_{tot} \sim d^2 \left(u_b + u_s\right) = \kappa \frac{H^2}{d^2} + T \frac{H^2 d^2}{R^2}. \tag{5.7}$$

Note that the bending energy decreases with the bulge size d, while the stretching energy increases with d. To determine the equilibrium shape of the shell, it is clear that both bending and stretching must be taken into account.

To find d, we consider Gibbs free energy,

$$G = U - p\Delta V, \tag{5.8}$$

where p is the pressure and ΔV is the change in volume due to the deformation. This volume scales as $\Delta V \sim Hd^2$, so

$$G \sim \left(\frac{TH^2}{R^2} - pH \right) d^2 + \kappa \frac{H^2}{d^2}, \tag{5.9}$$

so the effect of the pressure is to renormalise the parameter T to $\tilde{T} = T - \frac{pR^2}{H}$. Minimising the free energy with respect to d we find

$$0 = \frac{\partial G}{\partial d} \sim \tilde{T} \frac{dH^2}{R^2} - \kappa \frac{H^2}{d^3} \Rightarrow d \sim \left(\frac{\kappa}{\tilde{T}} \right)^{1/4} R^{1/2}. \tag{5.10}$$

Inserting this into the free energy, we find

$$U_{tot} \sim \sqrt{\kappa \tilde{T}} \frac{H^2}{R}, \tag{5.11}$$

and the work done by the pressure is

$$p\Delta V \sim pHR \frac{\kappa^{1/2}}{\tilde{T}^{1/2}}. \tag{5.12}$$

Once again minimising Gibbs free energy, this time with respect to H, we find

$$0 = \frac{\partial G}{\partial H} = \left(\frac{H}{R} \sqrt{\kappa \tilde{T}} - pR \frac{\kappa^{1/2}}{\tilde{T}^{1/2}} \right) + \left(\frac{H^2}{R} \frac{\kappa^{1/2}}{\tilde{T}^{1/2}} + pHR \frac{\kappa^{1/2}}{\tilde{T}^{3/2}} \right) \frac{\partial \tilde{T}}{\partial H}. \tag{5.13}$$

Inserting $\frac{\partial \tilde{T}}{\partial H} = p\frac{R^2}{H^2}$, we find

$$0 = \left(\frac{H}{R} \sqrt{\kappa \tilde{T}} - pR \frac{\kappa^{1/2}}{\tilde{T}^{1/2}} \right) + pR \frac{\kappa^{1/2}}{\tilde{T}^{1/2}} + \frac{p^2 R^3}{H} \frac{\kappa^{1/2}}{\tilde{T}^{3/2}}, \tag{5.14}$$

which gives

$$H \sim \frac{pR^2}{\tilde{T}} = \frac{pR^2}{T - \frac{pR^2}{H}}. \tag{5.15}$$

Solving this equation for H finally gives

$$H \sim \frac{pR^2}{T}. \tag{5.16}$$

This is the scaling of the depth of the deformation as a function of the applied pressure. The situation described above ceases to be valid if the forces on the membrane are so large that the shape of the membrane changes considerably. In this case, we assume that the bulge forms a mirror reflection of its original surface in a plane perpendicular to the symmetry axis. This means that well inside the bulge, the curvature of the deformed shell is opposite in sign but equal in magnitude to the curvature of the original surface, and hence the free energy density here remains unaffected. Instead, the major part of the change in free energy will be concentrated to a narrow strip of width δ around the edge of the bulge. The radius of the bulge is denoted r, and its depth H. We start by finding δ, once again through minimisation of Gibbs free energy.

The bending energy density is again given by

$$u_b \sim \kappa \frac{\xi^2}{\delta^4}, \tag{5.17}$$

and the stretching by

$$u_s \sim T \frac{\xi^2}{R^2}. \tag{5.18}$$

The area of the bending strip scales as $r\delta$, so the total elastic energy becomes

$$U_{tot} = r\delta \left(\kappa \frac{\xi^2}{\delta^4} + T \frac{\xi^2}{R} \right). \tag{5.19}$$

The deflection ξ is determined geometrically. With the notation defined in figure 5.5, we have $\xi = \delta \sin\alpha \approx \delta \frac{r}{R}$.

The total elastic energy thus becomes

$$U_{tot} \sim \kappa \frac{r^3}{R^2\delta} + T \frac{r^3\delta^3}{R^4}. \tag{5.20}$$

The work done by the pressure is again

$$W = p\Delta V \sim pHr^2. \tag{5.21}$$

Note that the work done by the pressure does not depend on the width of the bending strip δ; hence, in determining δ only the elastic free energy needs to be considered,

$$0 = \frac{\partial U_{tot}}{\partial \delta} \sim r^3 \left(T \frac{\delta^2}{R^4} - \kappa \frac{1}{R^2 \delta^2} \right) \to \delta \sim \frac{\kappa^{1/4}}{T^{1/4}} R^{1/2}. \tag{5.22}$$

Before we write down Gibbs free energy, we note that r and H are related geometrically through $r^2 \sim RH$. Then, minimising Gibbs free energy with respect to H we find

$$0 = \frac{\partial G}{\partial H} = \frac{\kappa^{3/4} T^{1/4} H^{1/2}}{R} - pRH, \tag{5.23}$$

which gives

$$H \sim \frac{\kappa^{3/2} T^{1/2}}{R^4 p^2}. \tag{5.24}$$

The physical interpretation of this result is that, if one decreases the pressure, the bulge will increase in size; this indicates that the structure is unstable. Indeed, calculating the seond derivative of Gibbs free energy one finds

$$\frac{\partial^2 G}{\partial H^2} = \frac{\kappa^{3/4} T^{1/4}}{2RH^{1/2}} - pR = -\frac{pR}{2} < 0, \tag{5.25}$$

meaning that this value of H corresponds to a maximum of Gibbs free energy, not a minimum. Larger bulges will grow on their own accord, while smaller bulges will decrease. It is therefore expected that until the critical bulge size H is reached, the deformation is well described by the scaling derived in the previous section,

$$H \sim \frac{pR^2}{T}. \tag{5.26}$$

So at what pressure does H reach its critial value? We set $H = H_{cr}$, giving

$$\frac{p_{cr} R^2}{T} = \frac{\kappa^{3/2} T^{1/2}}{R^4 p_{cr}^2} \Rightarrow p_{cr} \sim \frac{\sqrt{\kappa T}}{R^2}, \tag{5.27}$$

giving the correct scaling behavior.

The same method can be applied to doubly clamped beams with principal radii of curvature R_x and R_y. In this case, the stretching energy is expected to scale with the gaussian curvature, so

$$u_s = T \frac{\xi^2}{R_x R_y}. \tag{5.28}$$

Hence, for small deflections it is sufficient to do the substitiution $R^2 \to R_x R_y$, resulting in

$$H \sim \frac{pR_x R_y}{T}. \tag{5.29}$$

For large deflections, the situation is slightly more intricate. One can no longer assume that the bulge formed in the ribbon is closed by a simply connected curve as depicted in figure 4. Let us instead investigate the limit where this edge consists of two parallel lines, separated by a distance $2r$.Again, we start by determining the width of the edge region, δ by minimising the free energy. The bending energy density is still

$$u_b \sim \kappa \frac{\xi^2}{\delta^4}, \tag{5.30}$$

while the stretching energy scales with the gaussian curvature, as argued above,

$$u_s \sim T \frac{\xi^2}{R_x R_y}. \tag{5.31}$$

The same geometrical argument as for the fully clamped structures give for the deflection

$$\xi \sim \delta \frac{r}{R_x}. \tag{5.32}$$

The area of the width region scales as $D\delta$, where D is the width of the ribbon, so the total elastic energy becomes

$$U_{tot} \sim D\delta \left(\kappa \frac{r^2}{\delta^2 R_x^2} + T \frac{r^2 \delta^2}{R_x^3 R_y} \right). \tag{5.33}$$

Minimising with respect to δ gives

$$\delta \sim \left(\frac{\kappa}{T} R_x R_y \right)^{1/4}, \tag{5.34}$$

where we have used $r^2 \sim HR_x$. Inserting this into the elastic energy yields

$$U_{tot} \sim \frac{\kappa^{3/4} T^{1/4} HD}{R_x^{5/4} R_y^{1/4}}. \tag{5.35}$$

The work done by the pressure is

$$W = p\Delta V \sim pHrD \sim pDH^{3/2} R_x^{1/2}, \tag{5.36}$$

again using $r^2 \sim HR_x$. Once again differentiating Gibbs free energy with respect to H we find

$$H_{cr} \sim \frac{\kappa^{3/2} T^{3/2}}{R_x^{7/2} R_y^{1/2} p^2}, \tag{5.37}$$

where the subscript cr indicates that this is again the critical deformation of the shell. Using the scaling for small deformations found previously, $H \sim \frac{pR_xR_y}{T}$, we obtain the critical pressure

$$p_{cr} \sim \frac{\kappa^{1/4} T^{1/4}}{R_x^{3/2} R_y^{1/2}}. \tag{5.38}$$

If the pressure is applied electrostatically, we expect that $p \sim V^2$, meaning that the critical voltage would be given by

$$V_{cr} \sim \frac{\kappa^{1/4} T^{1/4}}{R_x^{3/4} R_y^{1/4}}. \tag{5.39}$$

Plotting V_{cr}^4 versus R^{-4} in a logarithmic scale for the fully clamped structures, the experimental values are expected to fall along a straight line with unit slope. The bending rigidity can then be extracted from the intersection of the line with the $y-$axis. The experimentally obtained values for the fully clamped structures, all bilayers, are shown in figure 5.7. It is seen that the scaling is very consistent with the one derived above. Using the analytical expression from Pogorelov, we were able to fit the bending rigidity, giving $\kappa \approx 30^{+20}_{-15}$eV. The rather large error bars here are mainly due to the smallness of the data set considered, and are not inherent to the method itself.

For the beam structures, the data points are expected to fall along a line with unit slope when plotting V_{cr}^4 versus R^{-3}. Also the beam structures follow the expected scaling, as seen in figure 5.7. In this data set both bilayers and monolayers are present. Using the value of the bending rigidity extracted for the bilayers, we found a monolayer bending rigidity of $\kappa \sim 7^{+4}_{-3}$ eV. Again, the error bars are large mainly due to the very small data set (only two monolayered structures were successfully fabricated and measured).

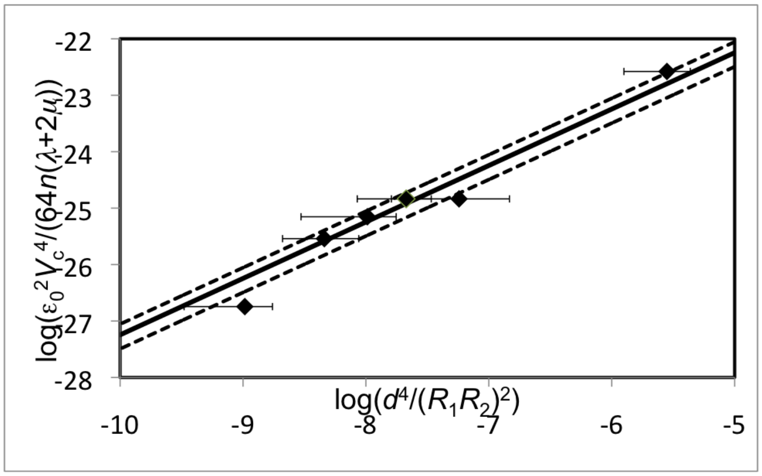

Figure 5.6: Scaling of the snap-through voltage with radius of curvature for fully clamped bilayer drums. The full line is the best least squares fit to the logarithmised values, while the dashed lines represent the uncertainty. The scaling is consistent with theoretical considerations.

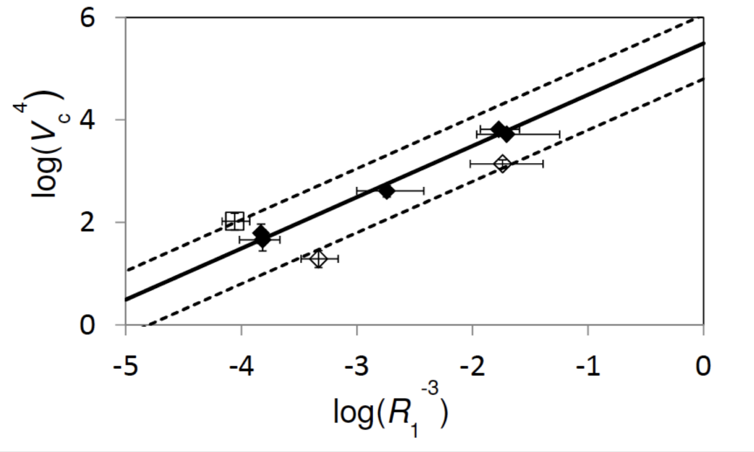

Figure 5.7: Scaling of the snap-through voltage with radius of curvature for doubly clamped beams. The open diamonds are monolayers, full diamonds bilayers and open square trilayer. The scaling is consistent with theoretical considerations.

Chapter 6

Summary and outlook

In this thesis, the equations of classical elasticity theory are applied to suspended graphene structures of various designs. In the first paper, a mechanically active suspended graphene sheet is used as a top gate in a carbon nanotube field effect transistor (CNTFET). The mechanical motion of the graphene is shown to improve the characteristics of the CNTFET. Using a simplified equation of motion coupled to the the electronic properties of the semiconducting CNT channel, a quantitative analysis of the performance of the device was made. The analysis focussed on the subthreshold slope of the device, a measure of the change in current due to a change in voltage close to the the switching of the transistor. It was found that there are two important parameters determining the subthreshold slope in these devices; first, the suspension height of the graphene and second, the initial tension of the graphene sheet. With a lower suspension height the capacitance between the graphene gate and the CNT channel increases, leading to a higher sensitivity to a change in voltage. For a given suspension height, there was also found to exist an optimum value of the tension of the sheet. Too high tension and the graphene gate does not respond well mechanically to an applied voltage. Too low tension and the graphene snaps in to the back gate before reaching the switching. The modeling was done in connection with experimental fabrication and characterisation of a device with the same design by an experimental group at Gothenburg University.

In an ongoing project, a more complete description of the elastic properties of graphene is employed to investigate the dissipation in suspended graphene structures arising from the coupling between the out-of-plane and in-plane motion of graphene. It was found that both linear and nonlinear (amplitude dependent) damping is expected to be present in such devices. The nonlinear damping is a result of the nonlinear coupling between the two systems. Although this nonlinear term was found too small to dominate the nonlinear response of suspended graphene sheets under realistic assumptions, it can, under certain circumstances, be the dominating dissipation term. More specifically, the ratio between the nonlinear and linear damping terms scale as $\frac{|\psi|^2}{\bar{q}^2}$, where ψ is the amplitude of the vibrational motion, and $\bar{q}$ is the static displacement of the graphene sheet. Thus, the nonlinear damping can dominate for small static displacements. The quality factor display qualitatively different behaviour with respect to driving voltage and bias voltage in the two different damping regimes. The quality factors obtained from this mechanism ranges from 10^4 to 10^6 for the considered geometry, which is consistent with recent experimental findings [18].

In the last paper, the bending rigidity of monolayer and bilayer graphene is estimated using suspended graphene sheets that are buckled due to a built-in compressive strain, fabricated and characterised by an experimental group at Gothenburg University. These structures were shown to display a snap-through instability under large enough pressures. Describing the buckled graphene sheet as a shallow elastic shell, the critical pressure could be related to the bending rigidity of the system. The bending rigidity of bilayered graphene was estimated to $\kappa \approx 30^{+20}_{-15}$ eV, and for monolayers to $\kappa \sim 7^{+4}_{-3}$ eV.

Bibliography

[1] H. W. Kroto, J. R. Heath, S. C. O'Brien, R. F. Curl, and R. E. Smalley, "C60: Buckminsterfullerene," *Nature*, vol. 318, pp. 162–163, 11 1985.

[2] S. Iijima and T. Ichihashi, "Single-shell carbon nanotubes of 1-nm diameter," *Nature*, vol. 363, pp. 603–605, 06 1993.

[3] M. Monthioux and V. L. Kuznetsov, "Who should be given the credit for the discovery of carbon nanotubes?," *Carbon*, vol. 44, no. 9, pp. 1621 – 1623, 2006.

[4] K. S. Novoselov, A. K. Geim, S. V. Morozov, D. Jiang, Y. Zhang, S. V. Dubonos, I. V. Grigorieva, and A. A. Firsov, "Electric field effect in atomically thin carbon films," *Science*, vol. 306, no. 5696, pp. 666–669, 2004.

[5] A. N. Obraztsov, "Chemical vapour deposition: Making graphene on a large scale," *Nat Nano*, vol. 4, pp. 212–213, 04 2009.

[6] A. H. Castro Neto, F. Guinea, N. M. R. Peres, K. S. Novoselov, and A. K. Geim, "The electronic properties of graphene," *Rev. Mod. Phys.*, vol. 81, pp. 109–162, Jan 2009.

[7] A. S. Mayorov, R. V. Gorbachev, S. V. Morozov, L. Britnell, R. Jalil, L. A. Ponomarenko, P. Blake, K. S. Novoselov, K. Watanabe, T. Taniguchi, and A. K. Geim, "Micrometer-scale ballistic transport in encapsulated graphene at room temperature," *Nano Letters*, vol. 11, no. 6, pp. 2396–2399, 2011.

[8] L. A. Ponomarenko, A. K. Geim, A. A. Zhukov, R. Jalil, S. Morozov, K. S. Novoselov, I. V. Grigorieva, E. H. Hill, V. V. Cheianov, I. V. Falko, K. Watanabe, T. Taniguchi, and R. V. Gorbachev, "Tunable

metal-insulator transition in double-layer graphene heterostructures," *Nature Physics*, 2011.

[9] Y. T. Yang, C. Callegari, X. L. Feng, K. L. Ekinci, and M. L. Roukes, "Zeptogram-scale nanomechanical mass sensing," *Nano Lett.*, vol. 6, no. 4, pp. 584–586, 2006.

[10] J. M. Kinaret, T. Nord, and S. Viefers, "A carbon nanotube-based nanorelay," *Appl.Phys.Lett*, vol. 82, p. 1287, 2003.

[11] H. J. Hwang and J. W. Kang, "Carbon-nanotube-based nanoelectromechanical switch," *Physica E*, vol. 27, p. 163, 2005.

[12] A. Isacsson, J. M. Kinaret, and R. Kaunisto, "Nonlinear resonance in a three-terminal carbon nanotube resonator," *Nanotech.*, vol. 18, 2007.

[13] V. Sasonova, Y. Yaish, H. Ustunel, D. Roundy, T. A. Arias, and P. L. McEuen, "A tunable carbon nanotube electromechanical oscillator," vol. 431, p. 284, 2004.

[14] T. Rueckes, K. Kim, E. Joselevich, G. Y. Tseng, C. L. Cheung, and C. M. Lieber, "Carbon nanotube-based nonvolatile random access memory for molecular computing," vol. 289, pp. 94–97, 2000.

[15] C. Stampfer, A. Jungen, R. Linderman, D. Obergfell, S. Roth, and C. Hierold, "Nano-electromechanical displacement sensing based on single-walled carbon nanotubes," *Nano Lett.*, vol. 6, no. 7, pp. 1449–1453, 2006.

[16] K.C.Schwab and M.L.Roukes, "Putting mechanics into quantum mechanics," *Physics Today*, 2005.

[17] D. Midtvedt, Y. Tarakanov, and J. Kinaret, "Parametric resonance in nanoelectromechanical single electron transistors," *Nano Letters*, vol. 11, no. 4, pp. 1439–1442, 2011.

[18] A. Eichler, J. Moser, J. Chaste, M. Zdrojek, I. Wilson-Rae, and A. Bachtold, "Nonlinear damping in mechanical resonators made from carbon nanotubes and graphene," *Nat Nano*, vol. 6, pp. 339–342, 06 2011.

[19] L. Britnell, R. V. Gorbachev, R. Jalil, B. D. Belle, F. Schedin, A. Mishenko, T. Georgiou, M. I. Katsnelson, L. Eaves, S. V. Morozov, N. M. R. Peres, J. Leist, A. K. Geim, and K. S. Novoselov, "Field-effect tunneling transistor based on vertical graphene heterostructures," *Science Express*, 2012.

[20] D. Yoon, Y.-W. Son, and H. Cheong, "Negative thermal expansion coefficient of graphene measured by raman spectroscopy," *Nano Lett.*, vol. 11, no. 8, pp. 3227–3231, 2011.

[21] L. Landau and E. Lifschitz, *Theory of Elasticity*, vol. 7. Elsevier, 3 ed., 1986.

[22] M. C. Cross and R. Lifshitz, "Elastic wave transmission at an abrupt junction in a thin plate with application to heat transport and vibrations in mesoscopic systems," *Phys. Rev. B*, vol. 64, p. 085324, Aug 2001.

[23] I. Wilson-Rae, "Intrinsic dissipation in nanomechanical resonators due to phonon tunneling," *Phys. Rev. B*, vol. 77, p. 245418, Jun 2008.

[24] R. Lifshitz and M. L. Roukes, "Thermoelastic damping in micro- and nanomechanical systems," *Phys. Rev. B*, vol. 61, Feb 2000.

[25] C. Seoánez, F. Guinea, and A. H. Castro Neto, "Dissipation in graphene and nanotube resonators," *Phys. Rev. B*, vol. 76, p. 125427, Sep 2007.

[26] R. Kubo, "The fluctuation-dissipation theorem," *Reports on Progress in Physics*, vol. 29, no. 1, p. 255, 1966.

[27] M. I. Dykman and M. A. Krivoglaz, "Theory of nonlinear oscillator interacting with a medium," *Soviet Scientific Reviews A*, vol. 5, pp. 265–441, 1984.

[28] K. F. Graff, *Wave motion in elastic solids.* Oxford: Dover, 1975.

[29] B. N. J. Persson, "Theory of rubber friction and contact mechanics," *J. Chem. Phys.*, vol. 115, no. 8, pp. 3840–3861, 2001.

[30] A. A. Maradudin and D. L. Mills, "The attenuation of rayleigh surface waves by surface roughness," *Appl. Phys. Lett*, vol. 28, no. 573-575, 1976.

[31] A. H. Nayfeh and D. T. Mook, *Nonlinear Oscillations.* Wiley-VCH, 1995.

[32] B. N. J. Persson and H. Ueba, “Heat transfer between weakly coupled systems: Graphene on a-sio2,” *EPL*, 2010.

[33] J. Atalaya, A. Isacsson, and J. M. Kinaret, “Continuum elastic modeling of graphene resonators,” *Nano Lett.*, vol. 8, no. 12, pp. 4196–4200, 2008.

[34] D.-B. Zhang, E. Akatyeva, and T. Dumitrică, “Bending ultrathin graphene at the margins of continuum mechanics,” *Phys. Rev. Lett.*, vol. 106, p. 255503, Jun 2011.

[35] Q. Lu, M. Arroyo, and R. Huang, “Elastic bending modulus of monolayer graphene,” *Journal of Physics D: Applied Physics*, vol. 42, p. 102002, 2009.

[36] A. Fasolino, J. H. Los, and M. I. Katsnelson, “Intrinsic ripples in graphene,” *Nat Mater*, vol. 6, pp. 858–861, 11 2007.

[37] K. V. Zakharchenko, J. H. Los, M. I. Katsnelson, and A. Fasolino, “Atomistic simulations of structural and thermodynamic properties of bilayer graphene,” *Phys. Rev. B*, vol. 81, p. 235439, Jun 2010.

[38] C. Lee, X. Wei, J. W. Kysar, and J. Hone, “Measurement of the elastic properties and intrinsic strength of monolayer graphene,” *Science*, vol. 321, no. 5887, pp. 385–388, 2008.

[39] R. Nicklow, N. Wakabayashi, and H. G. Smith, “Lattice dynamics of pyrolytic graphite,” *Phys. Rev. B*, vol. 5, pp. 4951–4962, Jun 1972.

[40] M. Poot and H. S. J. van der Zant, “Nanomechanical properties of few-layer graphene membranes,” *Applied Physics Letters*, vol. 92, pp. 063111 –063111–3, feb 2008.

[41] A. Pogorelov, *Bending of surfaces and stability of shells*, vol. 72. American Mathematical Society, 1 ed., 1988.